Electronic Supplementary Material (ESI) for New Journal of Chemistry.


# Structural, optical, dielectric and electrical transport property of a $[Mg(H_2O)_6]^{2+}$-templated proton conducting, semiconducting and photo responsive 3D Hydrogen bonded supramolecular framework

Soumen Singha,[1] Bhaskar Khanra,[1] Somen Goswami,[1] Rituparna Mondal,[1,2] Rajkumar Jana,[1,3] Arka Dey,[1] Sanjay Kumar Dey,[4] Partha Pratim Ray,[1] Corrado Rizzoli,[5] Rajat Saha,*[,6] Sanjay Kumar,*[,1]

[1]Department of Physics, Jadavpur University, Jadavpur, Kolkata-700032, WB, India
[2]Department of Electronics, Barrackpore Rastraguru Surendranath College, Barrackpore, West Bengal 700120, India
[3]Department of Physics, Techno India University, EM-4, Sector-V, Salt lake, Kolkata-700091, India
[4]Purulia Polytechnic, V. Nagar, Purulia, 723147, WB, India
[5]Dipartimento SCVSA, Università di Parma, Parco Area delleScienze 17/A, Parma, Italy
[6]Department of Chemistry, KaziNazrul University, Asansol-713340, WB, India

## EXPERIMENTAL SECTION

**General: Materials and Methods:** Co(II)-nitrate-hexahydrate, 2,5-pyridinedicarboxylic acid and magnesium nitrate-hexahydrate were purchased from Merck chemical company. All other chemicals used were of AR grade and used without any further purification. Elemental analysis (C, H, N) was performed by using a PerkinElmer 240C elemental analyzer. The thermogravimetric analysis was carried out to find out the thermal stability using a METTLER TOLEDO TGA/SDTA-851-e thermal analyzer under constant flow of $N_2$ (30 mL/min). The sample was heated up to 600°C at a rate of 10 °C/min in an inert alumina crucible. The Fourier transform infrared (FTIR) spectra of the complex between 450 and 4000 $cm^{-1}$ was collected in ATR mode by Shimadzu (Model – 8400S) FTIR Spectrophotometer using the KBr pellet method. The powder X-ray diffraction (PXRD) technique performing at ambient temperature (20 °C) was used to investigate the crystallinity

and phase purity of as synthesized bulk sample with a Bruker D8 powder X-ray Diffractometer operating in the reflection geometry using Cu Kα radiation (λ = 1.5418 Å) with the generator voltage and current set at 40 kV and 40 mA respectively. UV-visible-NIR (200-2000 nm) spectrum of the material (in solid powder form) in absorbance mode was recorded by using a Shimadzu UV-3101PC scanning spectrophotometer equipped with Integrating Sphere attachmentby Diffuse Reflectance technique. $BaSO_4$ powder was used as reference (100% reflectance). The spectra have been plotted as absorbance with respect to wavelength (λ in nm) and wave number ($\bar{\upsilon}_1$ in $cm^{-1}$) which is directly proportional to energy of the electronic transitions. For the practical application in fuel cell for the proton conductionin presence ofhumidityor in electrochemical appliances water stability of the material is very important. The solid crystalline material was powdered, soaked in water for three days and then filtered and dried in room temperature (25 °C). PXRD pattern was then recorded to determine the water stability of the powdered material.

**Synthesis of complex $\{[Co(2,5\text{-}Pdc)_2,(H_2O)_2]^{2-}.[Mg(H_2O)_6]^{2+}.4(H_2O)\}$:** At first equi-molar amount of $Na_2CO_3$ was added to a aqueous mixture of pyridine-2,5-dicarboxylic acid (2,5-Pdc) and stirred and heated to prepare the required disodium salt of pyridine-2,5-dicarboxylic acid ($Na_2$-2,5-Pdc). After obtaining the salt, equal volume of aqueous solutions were prepared for the three components e.g. disodium salt of pyridine-2,5-dicarboxylic acid ($Na_2$-2,5-Pdc) (0.0422 gm), $Mg(NO_3)_2{\cdot}6H_2O$ (0.051 gm) and $CoCl_2$ (0.024 gm) taken 2:2:1 ratio and mixed together to be of total 15 ml of solution of opaque orange in colour and the pH of the solution was maintained at 8. After stirring for 10 min the solution was transferred to a round bottom flask and refluxed at constant temperature of 90 °C for 3 hours and subsequently cooled down and filtered. As the filtrate was kept undisturbed in open air blocked shaped orange colored crystals start to appear after 3 days. After 10 days, single crystals suitable for single crystal X-ray (SCXRD) study were collected by filtration.Yield ~ 75%. Anal. Calc. (%) for

$C_{14}H_{30}CoMgN_2O_{20}$ (M = 629.24 g/mol): C, 26.7; H, 4.7 and N, 4.5 %. Found: C, 26.5; H, 4.6 and N, 4.4 %. Selected FT-IR bands (KBr pellet, $cm^{-1}$): $\nu_{asym}$ ($C{=}O_{stretchinguncoordinated}$) 1607(s), $\nu_{sym}$ ($C{=}O_{stretchinguncoordinated}$) 1391(s), $\nu_{asym}$ ($C{=}O_{stretchingcoordinated}$) 1592(s), $\nu_{sym}$ ($C{=}O_{stretchingcoordinated}$) 1361(s), ν(O-H) 3350(b).

**Single Crystal Data Collection and Refinement:** The Single Crystal X-ray Crystallographic data was recorded by mounting a suitable single crystal of the complex on a Bruker SMART APEX II CCD area-detector diffractometer equipped with a graphite monochromator, and Mo-$K_\alpha$ (λ = 0.71073 Å) radiation. The unit cell parameters were obtained from SAINT and absorption corrections were performed with SADABS. The structure was solved using Patterson method by using the SHELXS97. Subsequent difference Fourier synthesis and least-square refinement revealed the positions of the remaining non-hydrogen atoms. Non-hydrogen atoms were refined with independent anisotropic displacement parameters. Hydrogen atoms were placed in idealized positions and their displacement parameters were fixed to be 1.2 times larger than those of the attached non-hydrogen atom. Successful convergence was indicated by the maximum shift/error of 0.001 for the last cycle of the least squares refinement. All calculations were carried out using SHELXS 97,[1] SHELXL 97,[2] PLATON 99,[3] ORTEP-3[4] and WinGX system Ver-1.64.[5]

**Hirshfeld surface analysis:** Hirshfeld surface (HS) around a molecule can be constructed from the calculation of the electron density distribution around a molecule/moiety which in turn defines the shape of the molecule/moiety within the crystal system. For each point on the HS if, $d_e$ is the distance of the surface from the nearest atom external to the surface and $d_i$ is the analogous distance to the nearest atom internal to it then the normalized contact distance $d_{norm}$ can be expressed as $d_{norm}= \frac{(d_i - r_i^{vdW})}{r_i^{vdW}} + \frac{(d_e - r_e^{vdW})}{r_e^{vdW}}$, where $r_i^{vdW}$ and $r_e^{vdW}$ are the van der Waals radii of the appropriate atoms internal and external to the HS. By mapping the

functions like $d_i$, $d_e$, $d_{norm}$, shape index and curvedness on the HS and using proper colour scale structural information about the noncovalent interactions like π··· stacking and hydrogen bonding can be highlighted. The $d_{norm}$ mapped surface is generally visualized with the red–white–blue colouring scheme where the white areas correspond to the contacts with distances equal to the sum of the van der Waals radii of the atoms internal and external to the surface while bright red spots and blue coloured regions represent distances shorter (close contacts) and longer (distinct contact) than the sum of the van der Waals radii respectively. The two dimensional (2D) fingerprint plot (FP) of a molecular component as obtained from the HS analysis represents a 2D histogram plot with all possible $d_i$ and $d_e$ values around the molecular unit which can be and treated as a graphical 'summary' of all the contact distances to the HS. The FP can identify each type of intermolecular contacts within a supramolecular complex and their relative contributions to the HS can be obtained from the area of the surface. The shape index is very sensitive to any subtle changes in the shape of the surface, the red and blue triangles above the plane of the molecule denote the concave and convex regions indicating the atoms of the π··· stacked molecule above them and the atoms of the π··· ring inside the plane respectively. The Curvedness plot, which represents the measurement of "how much shape" can also reveal the π···π stacking interactions. Low values of curvedness lead to flat surface whereas high values of curvedness are correspond to the sharp curvature areas which tend to divide the surface into patches. These patches again can determine the interaction between neighboring moieties. The Hirshfeld surface plots and the associated 2D fingerprints of all component units have been calculated by using the Crystal Explorer package ver. 17.5[6] by importing the experimental structural data in CIF format.

**Intermolecular interaction energies calculation with energy framework representation:** The pair wise intermolecular interaction energies within a crystal were estimated following

the procedure of Tan and Tieknik[7] from a single-point molecular wave function at CE-B3LYP/6-31G(d,p)level on a cluster of radius 4 Å around each of the component of the complex. The interaction energies are consist of four energy components e.g. electrostatic ($E_{elec}$), polarization ($E_{pol}$), dispersion ($E_{dis}$) and exchange-repulsion ($E_{rep}$) energy and can be summed up as $E_{tot} = k_{ele}E_{elec} + k_{pol}E_{pol} + k_{dis}E_{dis} + k_{rep}E_{rep}$ where the k values are scaling factors.[8,9]

**Computational Details:** The optoelectronic behaviour of the complex has been probed by performing first principal calculation with periodic density functional theorem (DFT) utilizing the Cambridge serial total energy package (CASTEP) code.[10] The total energy, band structure (BS) and density of states (DOS), charge density, electron localization function (ELF) and partition of charges according to Mulliken[11] and Hirshfeld population analysis scheme were calculated on the experimentally obtained crystalline geometry.

**Band structure and Density of states:** From the calculation of total energy, Band Structure (BS), Density of states (DOS) have been found out. The following scheme was employed for every calculation.

i) As the atomic positions in the molecular geometry change and the cell dimensions or the quality of packing vary during the geometry optimization procedure, which in turn changes the intramolecular interactions, we choose to find out the electronic behaviour on the crystalline geometry of the complex and subsequent calculations were carried out on this model structure (Figure S11 (a)).

i) Basis set/Functional: Generalized Gradient Approximation (GGA)/Perdew-Burke-Ernzerhof (PBE) [12] exchange correlation functional(For energy calculation), GGA/PBE-Sol (For BS and DOS calculations),[13] An onsite Coulombic interaction of U=2.5 eV for the 3d electrons used in each of the calculations; ii) Pseudopotential representation: Reciprocal space iii) Pseudopotential: Ultrasoft;[14] iii) Kinetic cut-off energy for plane wave basis set

($E_c$): 380 eV; iv) k-point sampling scheme for the first Brillouin zone: Monkhorst-Pack;[15] v) k-point mesh: 2×2×1 (For energy calculation), 4×2×2 (For BS and DOS calculation); vi) Tolerance for SCF energy convergence: $5\times10^{-7}$ eV/atom; vii) Valence electronic configuration for pseudo atomic calculations: H-$1s^1$, C-$2s^2 2p^2$, N-$2s^2 2p^3$, O-$2s^2 2p^4$, Mg-$3s^2$and Co-$3d^7 4s^2$; viii) Method for long range dispersion correction: Grimme's DFT-D.[16]

**Optical properties study:** The prime aspect of the optical properties of any material is its dielectric function as it can describe optical response of the medium at all photon energies of the e. m. radiation due to the interaction the photons with electrons. Its imaginary part ε"(ω) can directly be derived from the electronic band structure of a material considering the interband optical transitions by estimating the dipole moment matrix elements between the occupied and unoccupied states (wave functions) within the selection rule. The real part ε'(ω) of the dielectric function can be derived from ε"(ω) by using the Kramers–Kronig relationship. All other important frequency dependent optical properties such as refractive index n(ω), extinction coefficient k(ω), absorption coefficient α(ω), optical conductivity σ(ω), reflectivity R(ω) and energy-loss function L(ω) can be extracted from the knowledge of both ε'(ω) and ε"(ω).[17-18]

**Dielectric property study:** The dielectric properties of complexwere measured by quasi-four probe method, using alternating current impedance spectroscopy (ACIS) technique, with the help of a computer-controlled LCR-meter (Agilent-4294A Precession Impedance Analyzer). For sample preparation, the complex was ground finely and then the powder was pelletized into a circular disc of thickness 1.55 mm by using a standard die of 8 mm and applying a pressure of 5 tons $cm^{-2}$ for 3 minutes followed by electrode deposition. The PXRD of the pellet was recorded and this pattern matches well with that of as synthesized sample (Figure S2 (c)). This indicates that the complex retains its structure after pelletisation. To develop

silver electrodes both flat surfaces of this disc were coated by highly pure Ag-paste and then the volatile thinner material (amile acetate) was removed by drying it at room temperature (298 K) in vacuum for 12 hours. The pellet was subjected to impedance analysis. The electrode assembly was kept in a closed glass container and was evacuated before measurement to remove moisture. The temperature of the oven was increased at a heating rate 0.5 °C/min. Each measured temperature was kept constant with an accuracy of ± 0.5 K. The frequency dependence of complex impedance and conductivity of the sample were recorded at different temperatures over a wide range of frequency (40Hz–5MHz) and within the temperature interval of 278K–343K using a computer-controlled LCR-meter (Agilent-4294A Precession Impedance Analyzer) under vacuum condition. The resistance was calculated by fitting the semicircle of the Nyquist plot. The activation energies were determined from the slope of Arrhenius plots.

**Electrical properties study:**

**Device fabrication:** Several metal-semiconductor (MS) junction devices were fabricated in ITO/complex/Al sandwich structure to perform the electrical study. In this regard, well dispersed solution of finely powdered sample was made in acetonitrile by mixing and sonicated the right proportion (25 mg/ml) of compound in a vial. This newly prepared stable dispersion of compound was deposited on the top of the ITO coated glass substrate by spun firstly at 600 rpm for 5 min and thereafter at 900 rpm for 6 min with the help of SCU 2700 spin coating unit. Afterward, all the as-deposited thin film was dried in a vacuum oven (at a base pressure of $5 \times 10^{-3}$ Torr) at room temperature for several minutes to evaporate the solvent part fully. The thicknesses of the developed film were measured by surface profiler as ~1 μm. The aluminium (Al) electrodes were deposited under base pressure ($10^{-6}$ Torr) by

maintaining the effective area as $7.065 \times 10^{-2}$ $cm^{-2}$ with shadow mask in the Vacuum Coating Unit 12A4D of HINDHIVAC.

**Electrical characterization and photo-responsivity study:** For electrical characterization of the device, the current-voltage (*I–V*) characteristics were measured under both dark condition and illumination (AM 1.5 G radiation) and recorded with the help of a Keithley2635B Source Measure Unit by two-probe technique. All the preparations and measurements were performed at room temperature and under ambient conditions.

**FIGURES**

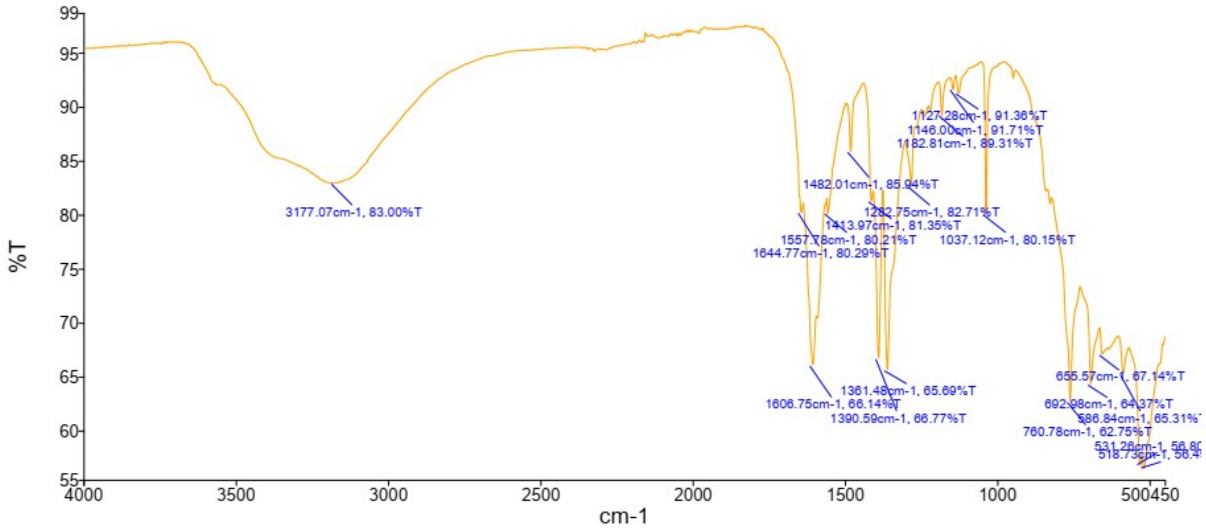


**Figure S1:** IR spectra of the complex.

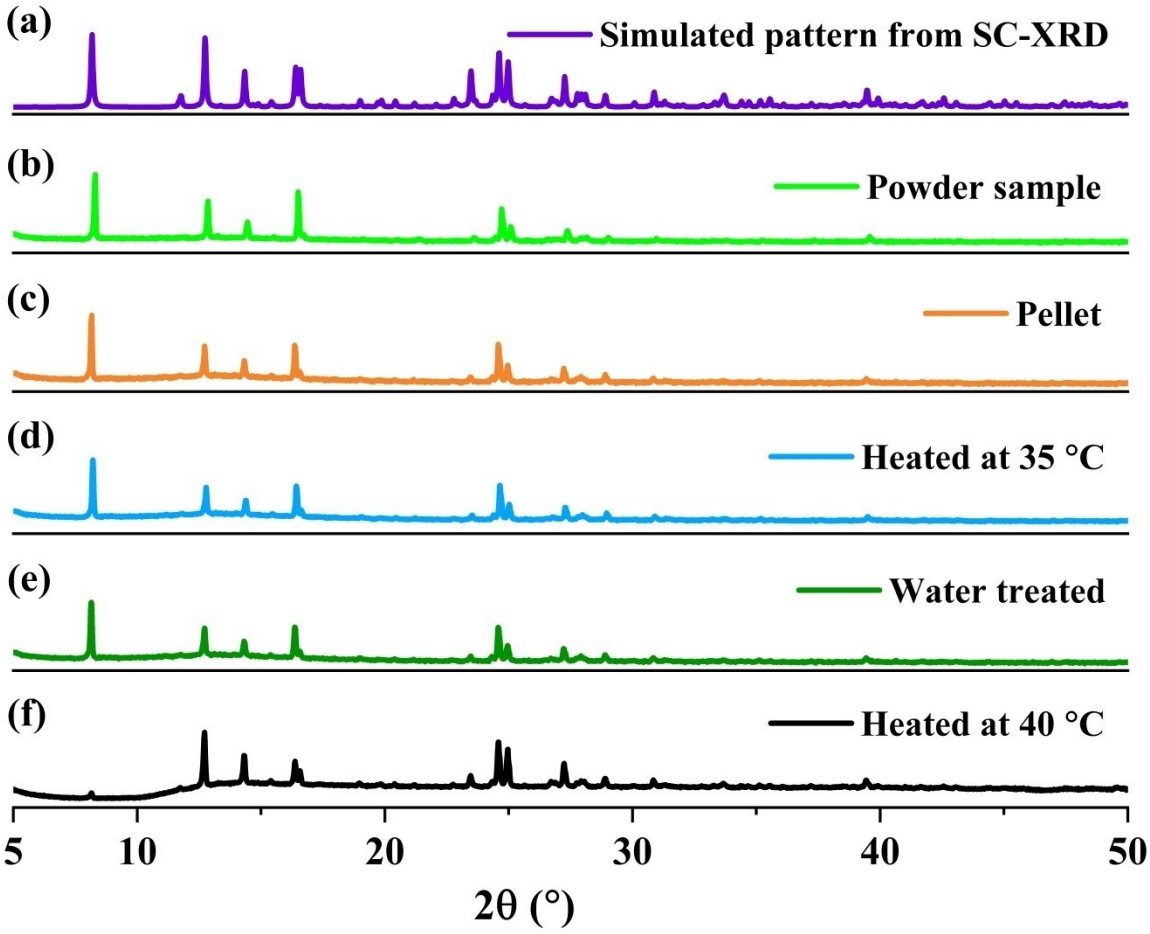

**Figure S2:** PXRD pattern of complex**.**

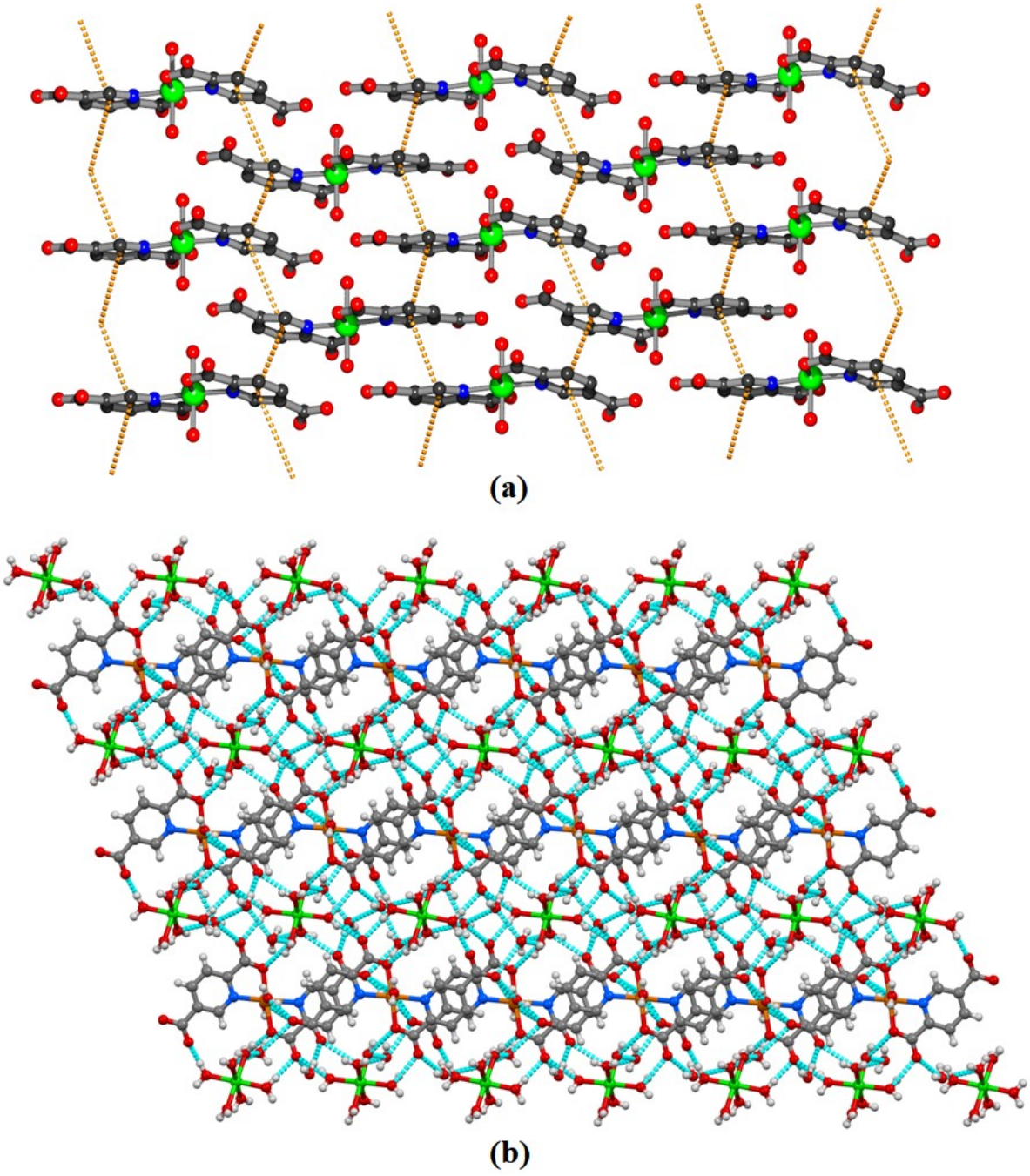


**Figure S3:** (a) 2D supramolecular sheets of $[Co(2,5\text{-}Pdc)_2.(H_2O)_2]^{2-}$ units in *ac*-plane supported by π···π interaction, (b) 3D supramolecular architecture of complex. (Hydrogen bonding interactions: Cyan dotted lines)

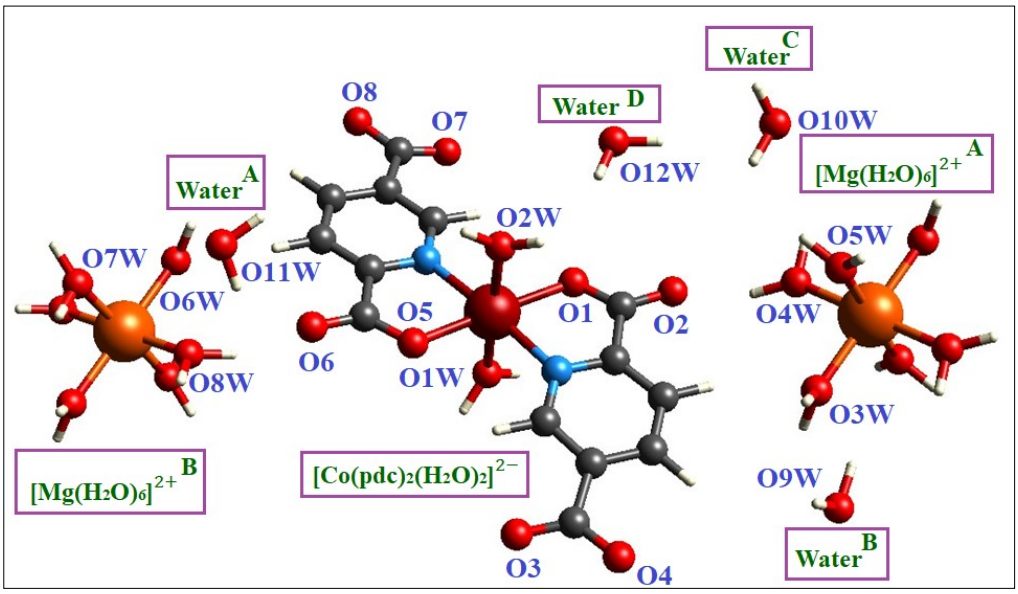


**Figure S4:** Components of the complex with their nomenclature used for HS, FP and intermolecular interaction energy analysis.

| | Molecular fragments | | | | | |
|---|---|---|---|---|---|---|
| **Properties** | $[Mg(H_2O)_6]^{2+}$ A | $[Mg(H_2O)_6]^{2+}$ B | Water A | Water B | Water C | Water D |
| $d_i$ | 0.7212 – 2.3164 Å | 0.7425 – 2.4464 Å | 0.7904 – 1.9760 Å | 0.8734 – 2.0292 Å | 0.7082 – 2.0401 Å | 0.7127 – 1.9551 Å |
| $d_e$ | 0.8744 – 2.2299 Å | 1.0087 – 2.3773 Å | 0.7137 – 2.2874 Å | 0.7216 – 2.3595 Å | 1.0343 – 2.4381 Å | 0.8186 – 2.3037 Å |
| $d_{norm}$ | -0.6312 – 1.4835 Å | -0.5961 – 1.2748 Å | -0.6431 – 1.0452 Å | -0.6281 – 1.1679 Å | -0.6497 – 1.0522 Å | -0.6435 – 1.0733 Å |
| Shape index | -1.0000 – 1.0000 Å | -1.0000 – 1.0000 Å | -1.0000 – 1.0000 Å | -1.0000 – 1.0000 Å | -1.0000 – 1.0000 Å | -1.0000 – 1.0000 Å |
| Curvedness | -4.0000 – 0.4000 Å | -4.0000 – 0.4000 Å | -4.0000 – 0.4000 Å | -4.0000 – 0.4000 Å | -4.0000 – 0.4000 Å | -4.0000 – 0.4000 Å |
| Fragment Patch | 0.0000 – 19.0000 Å | 0.0000 – 19.0000 Å | 0.0000 – 8.0000 Å | 0.0000 – 8.0000 Å | 0.0000 – 8.0000 Å | 0.0000 – 7.0000 Å |

**Figure S5:** Hirshfeld surface calculated over two cationic moieties and four guest water molecules mapped with specific properties (color scale are denoted in Å).

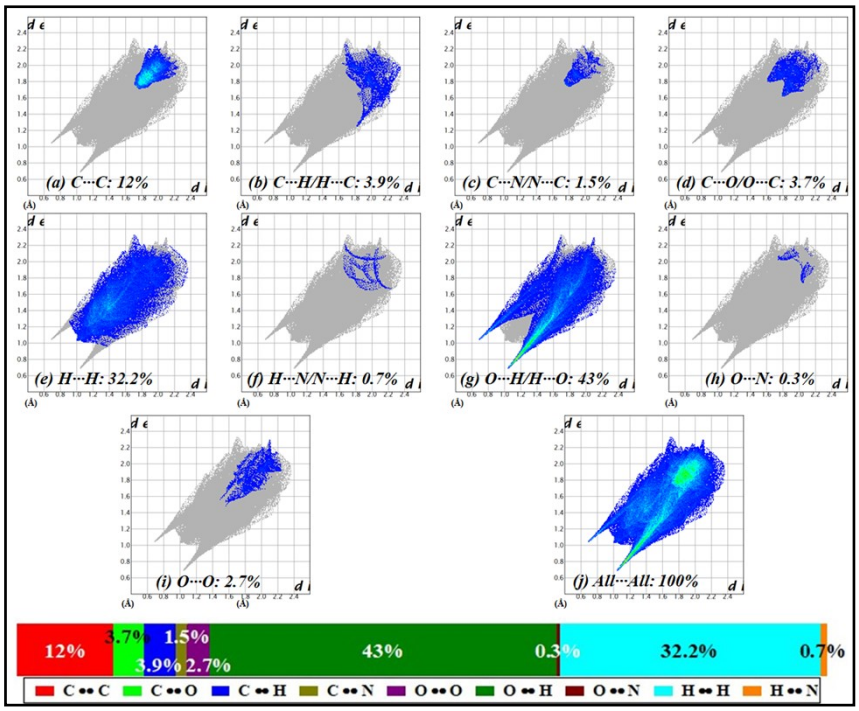


**Figure S6:** 2D fingerprint plot calculated for the HS over the anionic coordination moiety.

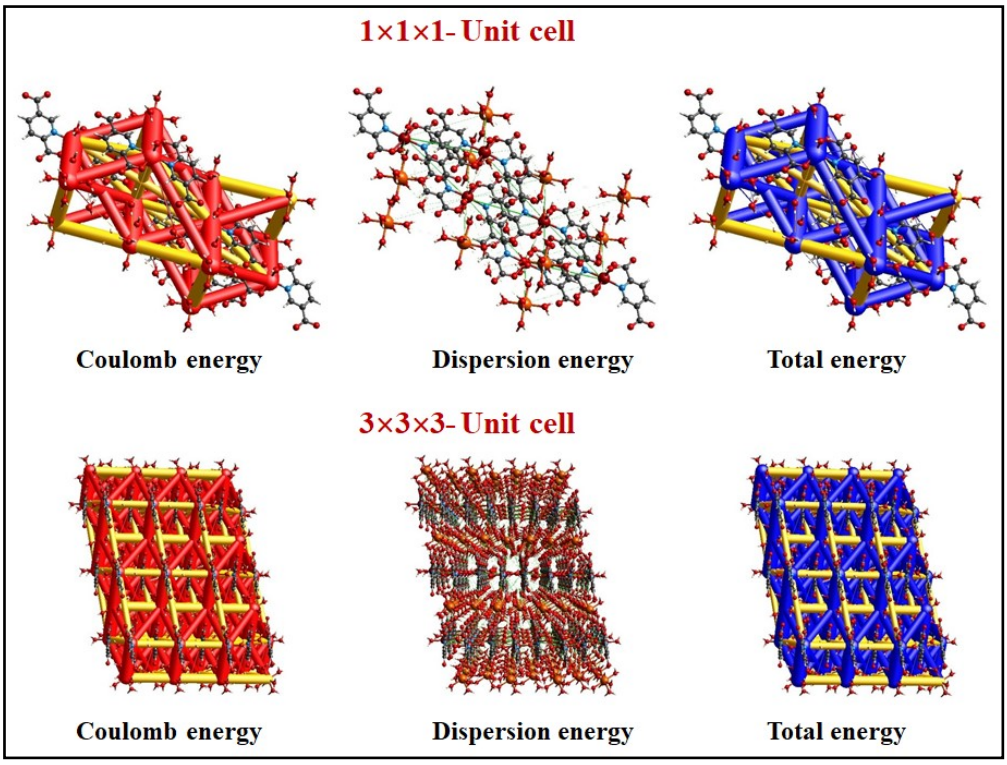


**Figure S7:** Overall view of the interaction energies over the 1×1×1 and 3×3×3 unit cell.

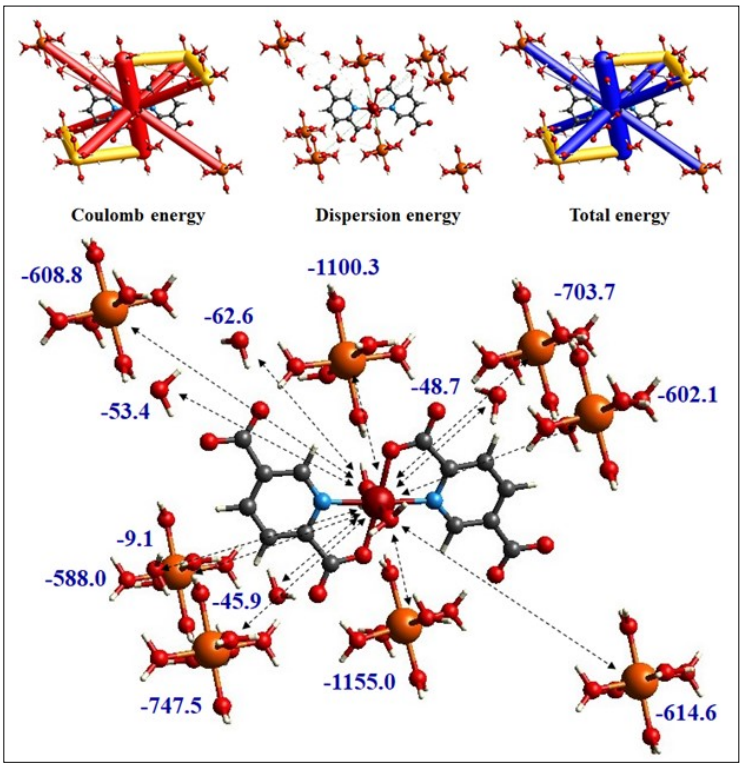


**Figure S8:** Interaction energies between the anionic unit and the rest of the components of the complex.

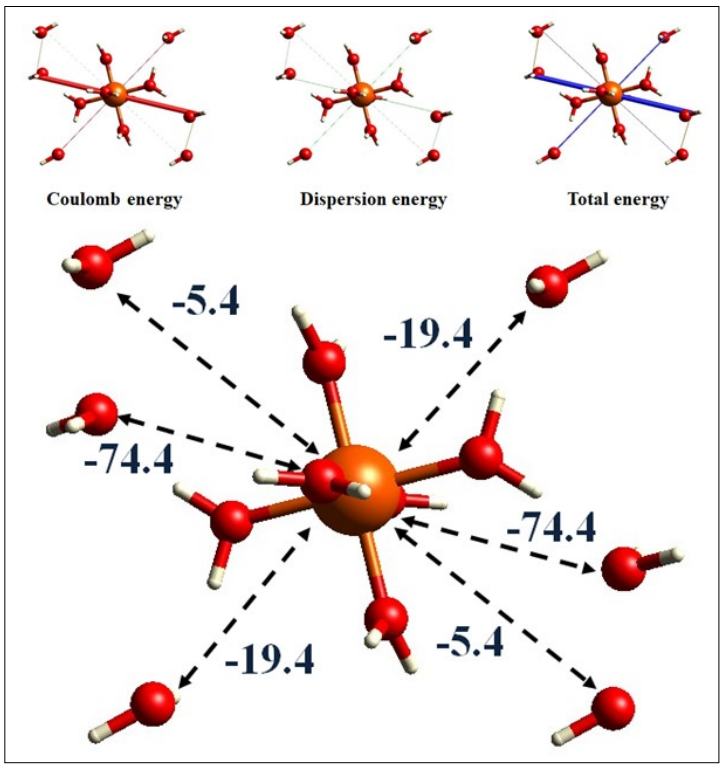


**Figure S9:** Interaction energies around the cationic unit $[Mg(OH)_6]^{2+}$ (A) with the guest water molecules.

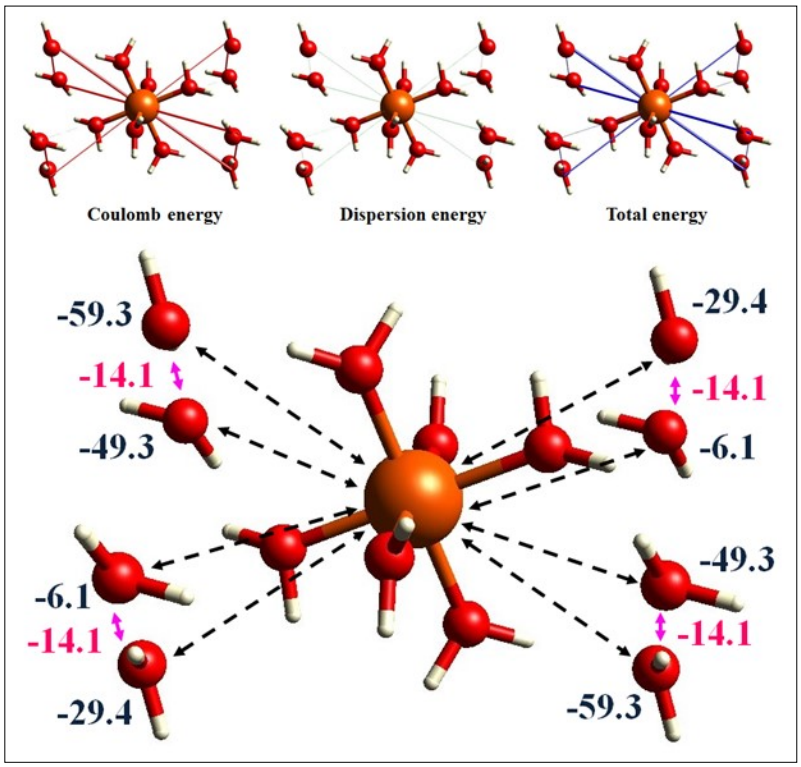


**Figure S10:** Interaction energies around the cationic unit $[Mg(OH)_6]^{2+}$ (B) with the guest water molecules.

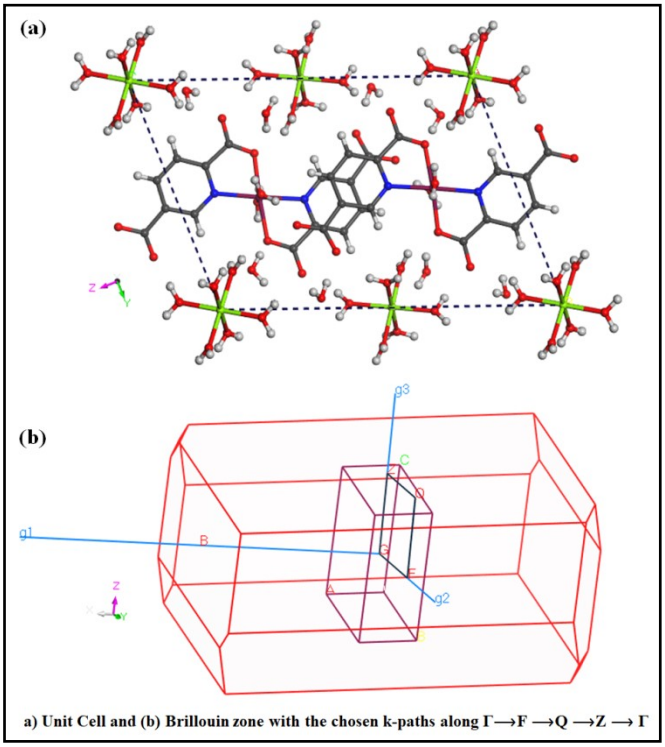


**Figure S11:** Real space and Reciprocal space lattice vectors, the Brillouin zone with chosen k-points and the model structure taken for calculations.

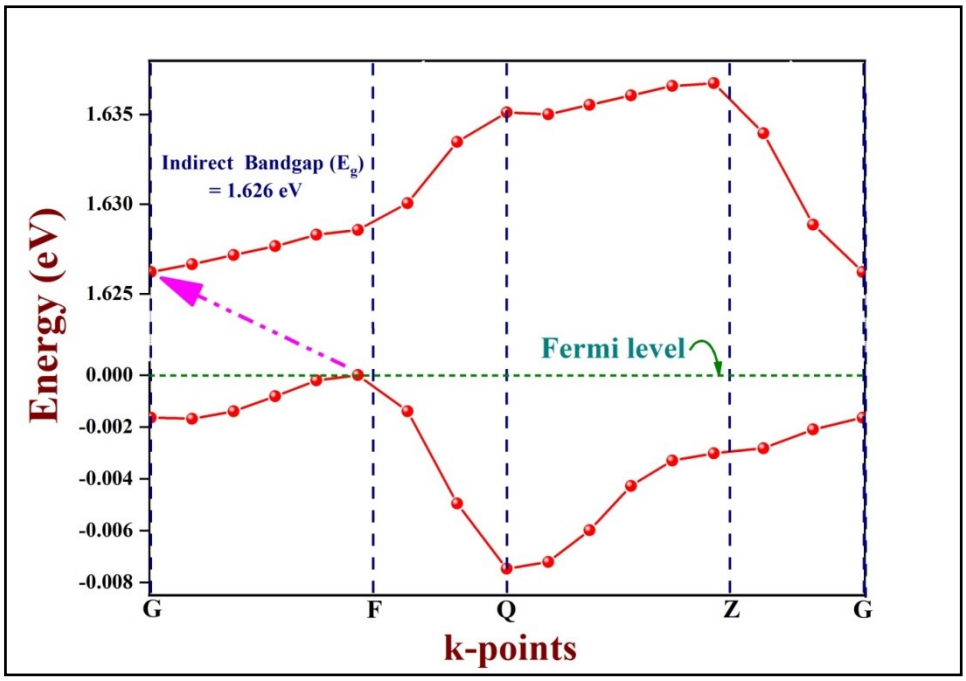


**Figure S12:** Band structure zoomed over valence band maxima and conduction band minima.

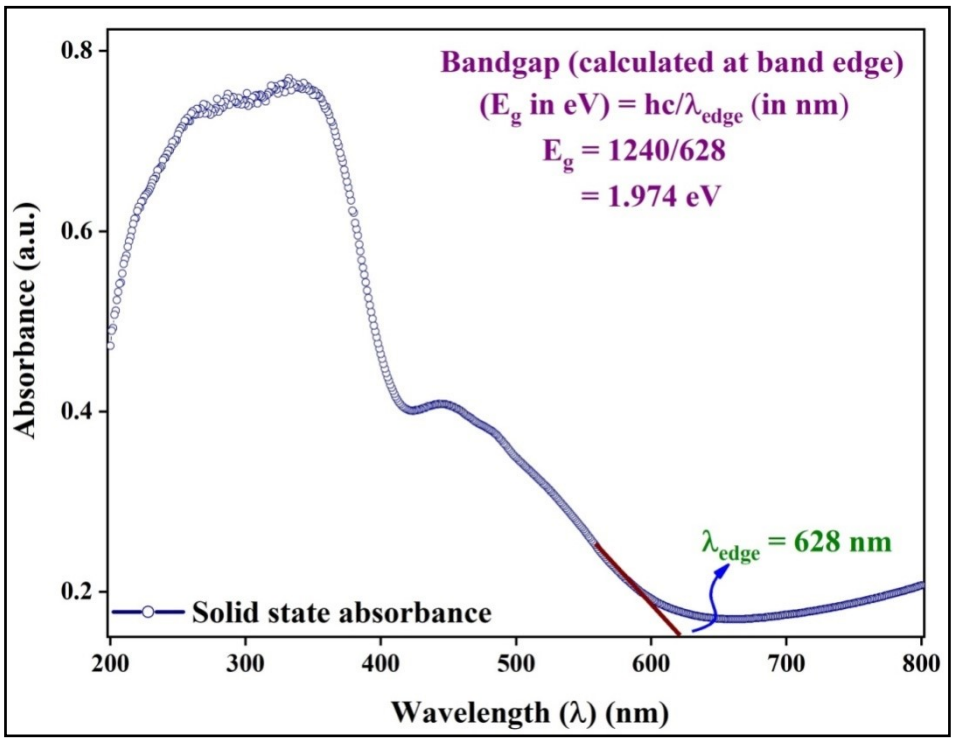


**Figure S13:** Solid state UV-DRS spectra and the optical bandgap of the complex.

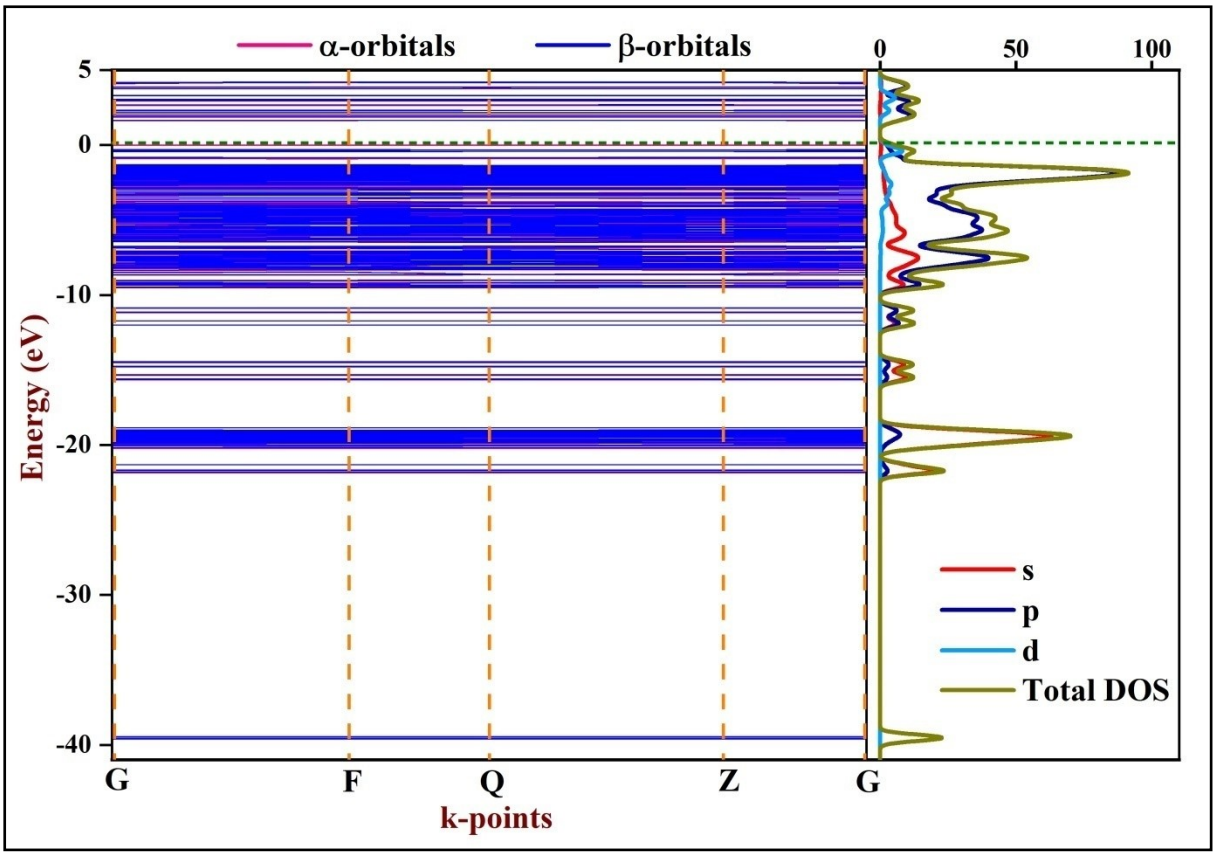


**Figure S14:** The Density of states assigned to each band of the calculated Band structure.

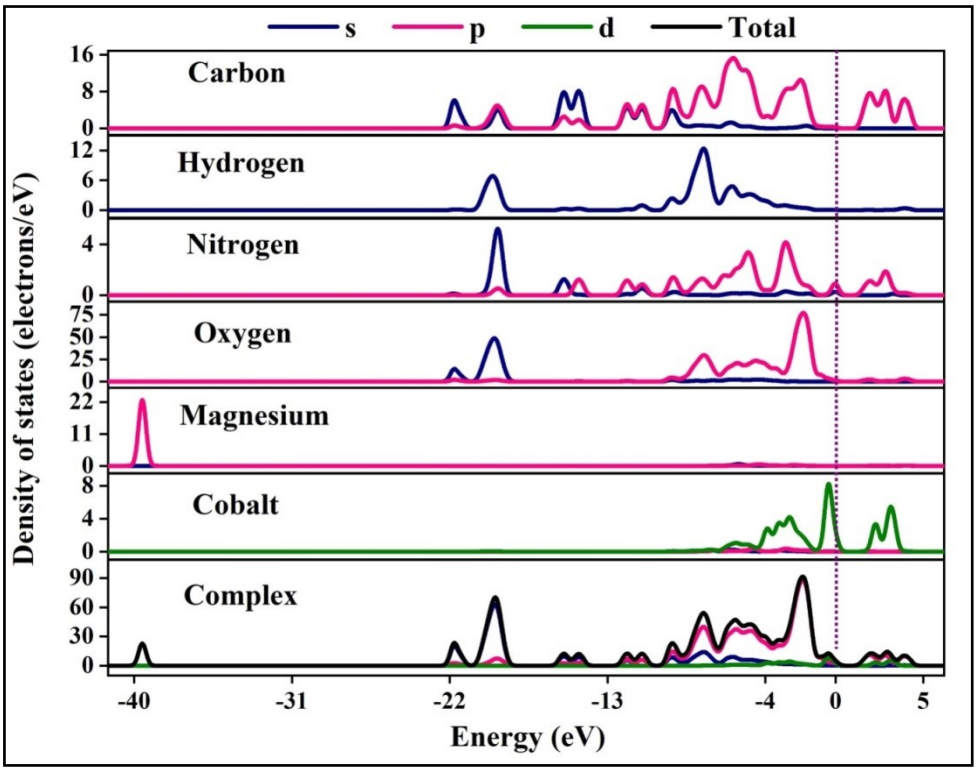


**Figure S15:** Total density of states (TDOS) of the sample and the atomic contributions from the constituent atoms forming the sample (PDOS).

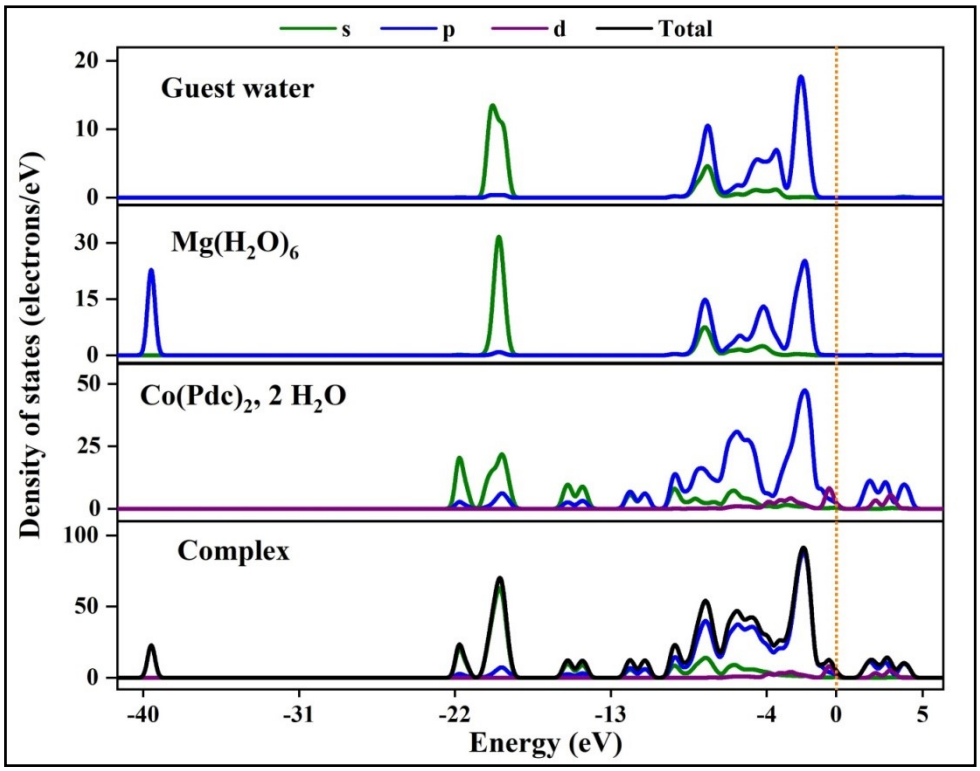


**Figure S16:** Total density of states of the supramolecular complex and the Partial density of states of the components.

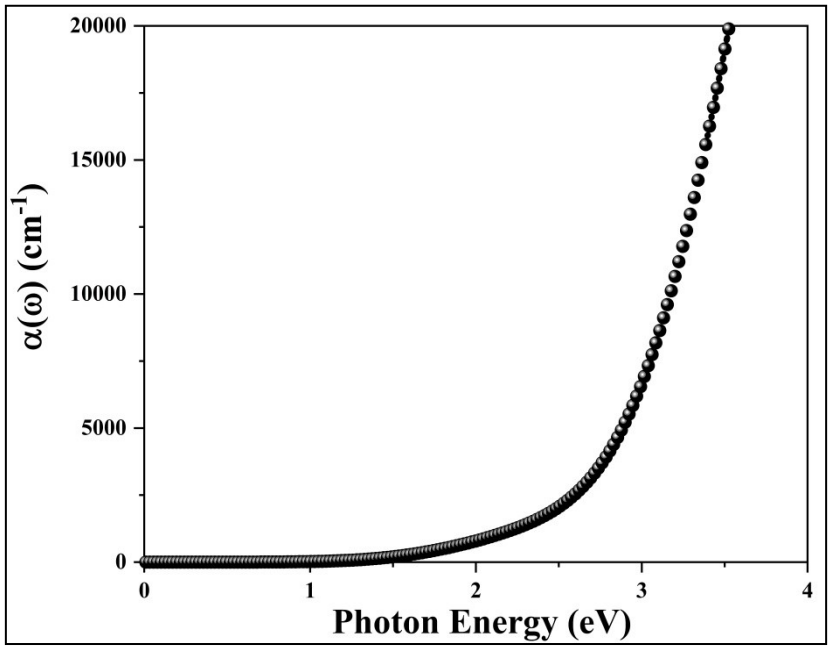


**Figure S17:** Absorption spectra zoomed over the energy range of the narrow visible and UV part of the electromagnetic radiation.

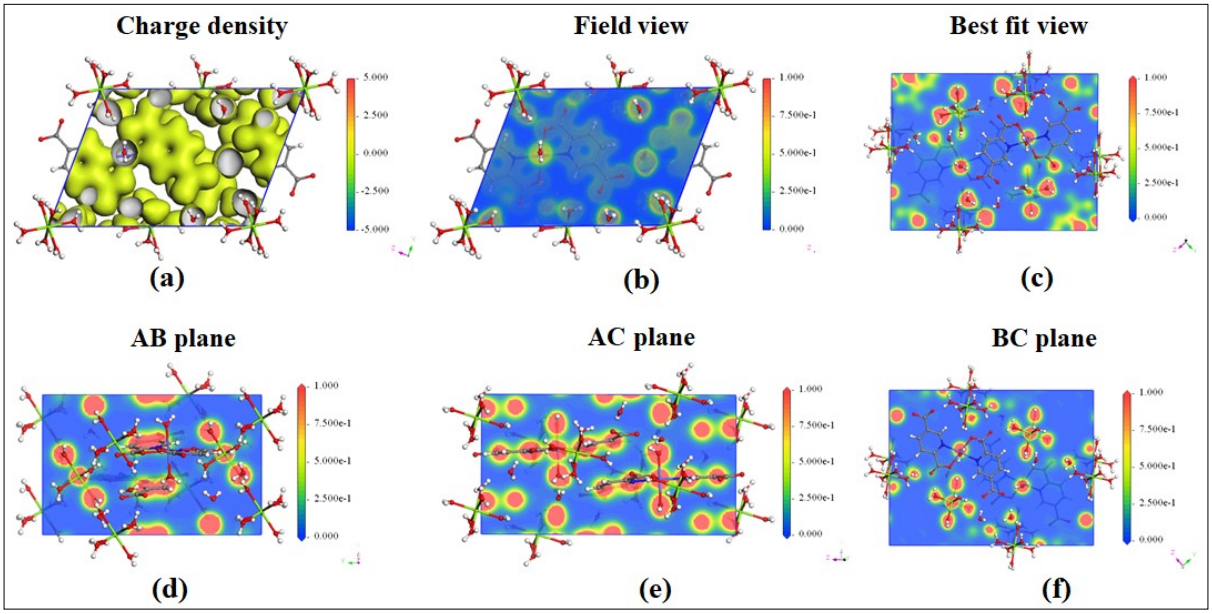


**Figure S18:** Calculated (a) electronic charge density isosurface, (b) field view (c) best fit view and charge density viewed on lattice plane with Miller indices (d) (0, 0, 1), (e) (0, 1, 0) and (f) (1, 0, 0) respectively.

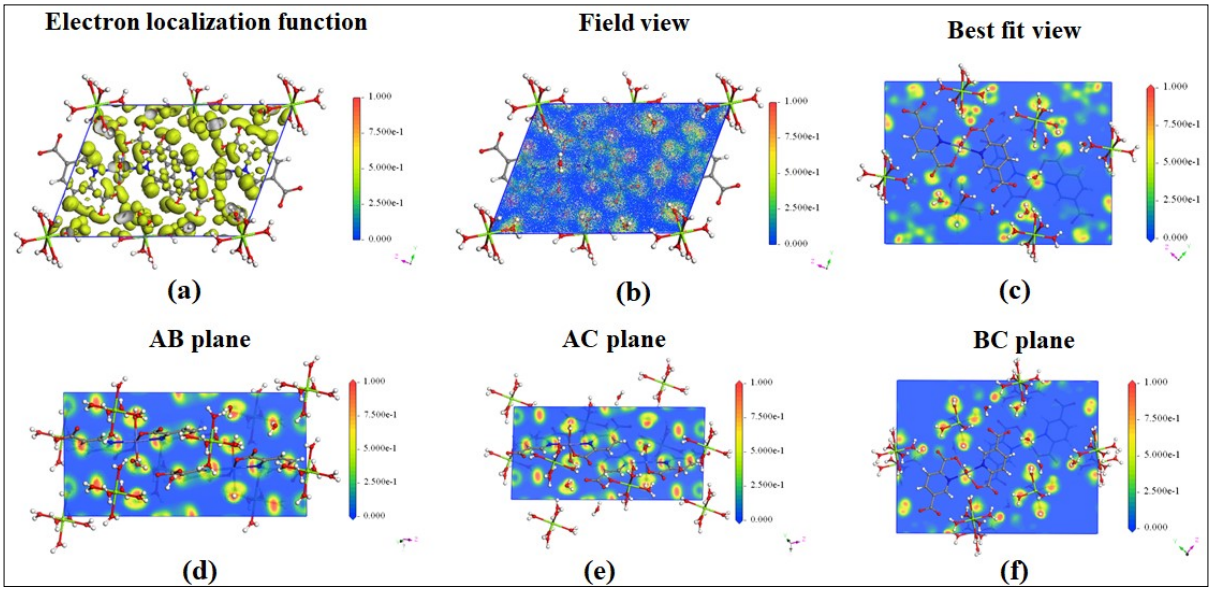

**Figure S19:** Calculated (a) Electron localization function (ELF) isosurface, (b) field view (c) best fit view and ELF viewed on lattice plane with Miller indices (d) (0, 0, 1), (e) (0, 1, 0) and (f) (1, 0, 0) respectively.

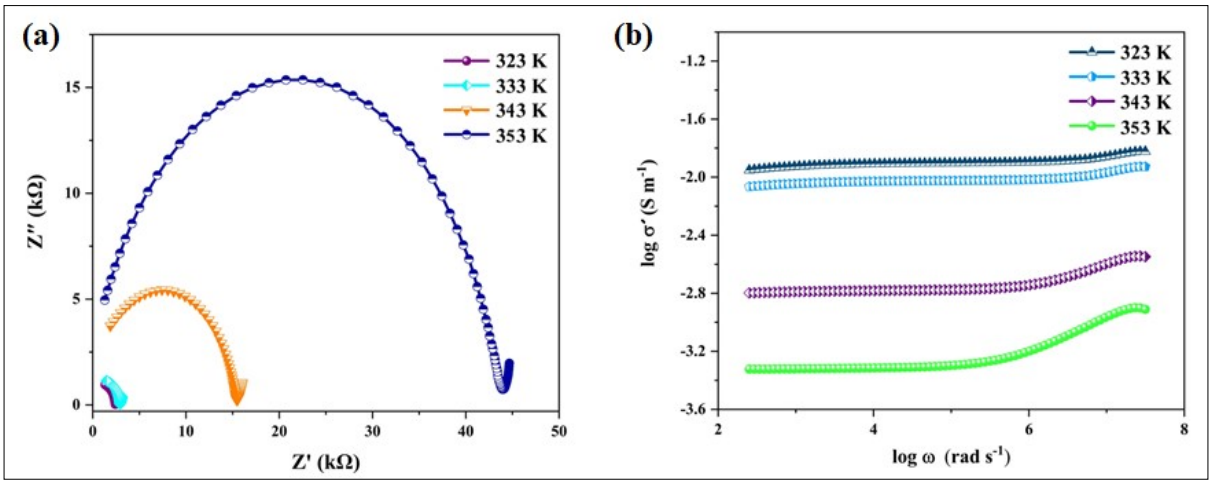


**Figure S20:** (a) Complex impedance spectra (Nyquist plot) and (b) Conductivity spectra of the complex within the temperature range of 323 K to 353 K.

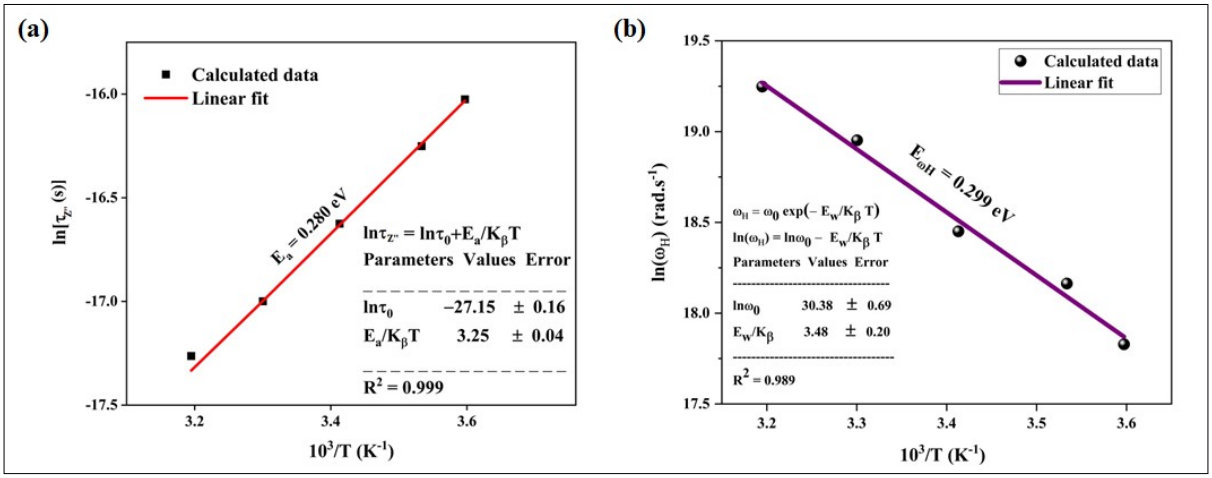


**Figure S21:** (a)Temperature dependence of the most probable relaxation time as obtained from the position of frequency dependent peaks of $Z''$ at different temperatures, (b) Variation of hopping frequency with temperature and the corresponding Arrhenius plot.

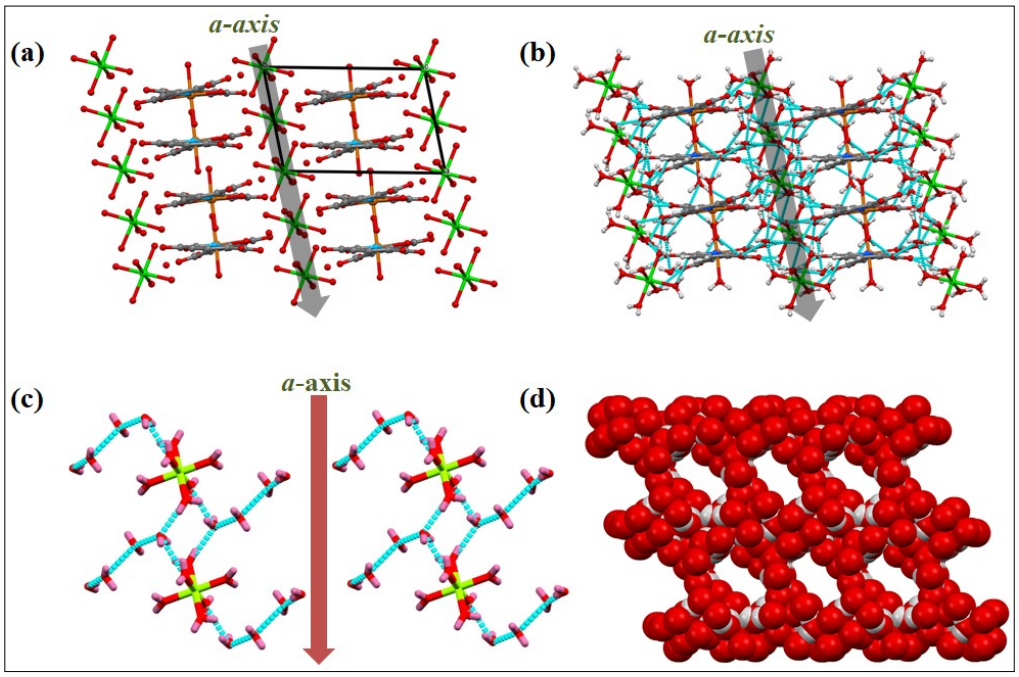


**Figure S22:** (a) and (b) The possible conduction pathway of the protons to migrate through the sample along *a*-axis; (c) the hydrogen bonding between the cationic unit and guest water molecules spanning along *a*-axis; (d) high concentration of oxygen atom within the supramolecular framework favorable for transporting the protons through the sample (red: oxygen, grey: hydrogen).

## TABLES

**Table S1:** Crystallographic data collection and refinement parameters of the complex.

| Identification code | Complex |
|---|---|
| Empirical formula | $[Co\{(C_7\ H_3NO_4)_2.2H_2O\}]^{2-}.[Mg(H_2O)_6]^{2+}.4(H_2O)$ |
| Formula weight | 629.64 |
| Crystal system | Triclinic |
| Space group | $P\bar{1}$ |
| Unit cell dimensions a (Å) | 7.3334(9) |
| b (Å) | 11.7205(15) |
| c (Å) | 16.2038(16) |
| α (º) | 109.468(7) |
| β (º) | 96.697(5) |
| γ (º) | 99.022(2) |
| V(Å$^3$) | 1275.4(3) |
| Z | 2 |
| Density (calculated) $\rho_{calc}$ (g/cm$^3$) | 1.640 |
| μ (Mo Kα) (mm$^{-1}$) | 0.791 |
| F(000) | 654 |
| Crystal type | Orange block shaped |
| Crystal size (mm$^3$) | 0.08 × 0.12 × 0.16 |
| Temperature (K) | 293 |
| θ range for data collection (°) | 1.4 - 28.6 |
| Total data | 17742 |
| Unique Data | 6417 |
| $R_{int}$ | 0.033 |
| Observed data [I > 2.0σ(I)] | 5723 |
| $N_{ref}$ | 6417 |
| $N_{par}$ | 346 |
| R | 0.0729 |
| $wR_2$ | 0.2023 |
| S | 1.16 |

$w = 1/[\sigma^2(Fo^2)+(aP)^2+bP]$ where $P=(Fo^2+2Fc^2)/3$

**Table S2:** Selected bond lengths (in Å), bond angles (in °) and dihedral angle (in °) for the complex.

| **Crystalline geometrical parameters** | | | |
|---|---|---|---|
| **Bond** | **Bond distance** | **Bond** | **Bond distance** |
| Co1−O1 | 2.093(4) | Mg2−O7W | 2.080(5) |
| Co1−O1W | 2.060(4) | Mg2−O8W | 2.066(3) |
| Co1−O2W | 2.033(4) | Mg2−O6W_b | 2.073(3) |
| Co1−O5 | 2.076(4) | Mg2−O7W_b | 2.080(5) |
| Co1−N1 | 2.119(3) | Mg2−O8W_b | 2.066(3) |
| Co1−N2 | 2.126(3) | C1−O1 | 1.268(6) |
| Mg1−O3W | 2.099(4) | C1−O2 | 1.245(6) |
| Mg1−O4W | 2.055(3) | C7−O3 | 1.239(6) |
| Mg1−O5W | 2.074(4) | C7−O4 | 1.262(6) |
| Mg1−O3W_a | 2.099(4) | C8−O5 | 1.268(6) |
| Mg1−O4W_a | 2.055(3) | C8−O6 | 1.244(6) |
| Mg1−O5W_a | 2.074(4) | C14−O7 | 1.225(6) |
| Mg2−O6W | 2.073(3) | C14−O8 | 1.277(6) |
| | | | |
| **Bond angle** | **Value** | **Bond angle** | **Value** |
| O1−Co1−O1W | 89.03(17) | O1W−Co1−N2 | 90.00(16) |
| O1−Co1−O2W | 88.66(17) | O2W−Co1−O5 | 88.84(17) |
| O1−Co1−O5 | 175.72(13) | O2W−Co1−N1 | 93.19(17) |
| O1−Co1−N1 | 77.48(13) | O2W−Co1−N2 | 89.95(17) |
| O1−Co1−N2 | 104.96(13) | O5−Co1−N1 | 99.19(13) |

| | | | |
|---|---|---|---|
| O1W−Co1−O2W | 177.59(19) | O5−Co1−N2 | 78.52(13) |
| O1W−Co1−O5 | 93.51(17) | N1−Co1−N2 | 176.09(14) |
| O1W−Co1−N1 | 86.97(16) | | |
| | | | |
| **Dihedral angle** | **Value** | **Dihedral angle** | **Value** |
| Pyridine···**P**yridine | 15.31 | C9−C8−O5−O6 | 179.56 |
| C2−C1−O2−O1 | 178.40 | C12−C14−O7−O8 | 178.54 |
| C5−C7−O3−O4 | 179.51 | N1−O1−N2−O5 | 4.44 |

Symmetry transformations used to generate equivalent atoms: (_a) 1-x,-y,1-z, (_b) -x,2-y,-z.

**Table S3:** π···π interaction parameters of the complex.

| **π···π interactions** | | | | | |
|---|---|---|---|---|---|
| $\boldsymbol{R_i \cdots R_j}$ | **symmetry equivalence** | $d[\boldsymbol{R_i \cdots R_j}]$ **(Å)** | **α (°)** | $d(\boldsymbol{R_i \cdots \perp R_j})$ **(Å)** | $d(\boldsymbol{R_j \cdots \perp R_i})$ **(Å)** |
| *R*1··· *R*1 | 1-x,1-y,1-z | 3.544(3) | 0.0(2) | 3.4558(19) | 3.4555(19) |
| *R*2··· *R*2 | -x,1-y,-z | 3.717(3) | 0.0(2) | -3.546(2) | -3.546(2) |
| *R*2··· *R*2 | 1-x,1-y,-z | 4.054(3) | 0.0(2) | 3.772(2) | 3.772(2) |

*R*1 (Cg1) and *R*2 (Cg2) are the centroids of the N1/C2/C3/C4/C5/C6 and N2/C9/C10/ C11/C12/C13 rings.

**Table S4:** *l.p.*⋯π interaction parameters of the complex.

| **C−O⋯$R_i$** | **symmetry equivalence** | ***d*[O⋯$R_i$] (Å)** | ***d* ⊥ [O⋯$R_i$] (Å)** | **γ (∠O⋯$R_i$ ⋯ ⊥ $R_i$) (°)** | **∠C−O⋯$R_i$ (°)** |
|---|---|---|---|---|---|
| C7−O3⋯*R*1 | -x,1-y,1-z | 3.872(5) | -3.397 | 28.64 | 70.0(3) |
| C7−O4⋯*R3* | -x,1-y,1-z | 3.824(5) | -3.731 | 12.68 | 99.8(3) |
| C7−O4⋯*R*3 | 1-x,1-y,1-z | 3.561(5) | 3.514 | 9.35 | 93.7(3) |
| C7−O4⋯*R*1 | -x,1-y,1-z | 3.877(5) | -3.733 | 15.67 | 69.8(3) |
| C14−O8⋯*R*4 | -x,1-y,-z | 3.589(4) | -3.555 | 7.88 | 84.1(3) |
| C14−O8⋯R4 | 1-x,1-y,-z | 3.781(4) | 3.762 | 5.76 | 100.3(3) |

*R*3 (*Cg*3)and*R*4 (*Cg*4) are the centroids of the Co1/O1/C1/C2/N1 and Co1/O5/C8/C9/N2.

**Table S5:** Hydrogen bonding interaction parameters of the complex.

| **Hydrogen bonding parameters** | | | | | |
|---|---|---|---|---|---|
| **D−H⋯A** | **Symmetry equivalence** | ***d*[D−H] (Å)** | ***d*[H⋯A] (Å)** | ***d*[D⋯A] (Å)** | **∠D−H⋯A(°)** |
| O1W−H371⋯O4 | -x,1-y,1-z | 0.85 | 2.30 | 2.759(6) | 114.0 |
| O1W−H372⋯O8 | -x,1-y,1-z | 0.85 | 2.30 | 2.677(6) | 132.0 |
| O2W−H381⋯O4 | 1-x,1-y,1-z | 0.85 | 1.87 | 2.686(6) | 161.0 |
| O2W−H382⋯O8 | 1-x,1-y,-z | 0.85 | 1.90 | 2.683(6) | 153.0 |
| O9W−H531⋯O3W | | 0.86 | 2.51 | 2.899(5) | 109.0 |
| O9W−H531⋯O8 | x,y,1+z | 0.86 | 2.36 | 2.851(5) | 117.0 |
| O9W−H532⋯O3W | | 0.85 | 2.46 | 2.899(5) | 113.0 |
| O10W−H541⋯O3 | 1-x,1-y,1-z | 0.86 | 1.89 | 2.750(7) | 173.0 |
| O10W−H542⋯O2 | 1+x,y,z | 0.87 | 1.99 | 2.852(7) | 169.0 |

| | | | | | |
|---|---|---|---|---|---|
| O11W−H551···O7 | 1-x,1-y,-z | 0.86 | 2.34 | 3.137(7) | 154.00 |
| O11W−H552···O6 | | 0.86 | 2.02 | 2.746(7) | 142.0 |
| O12W−H562···O4 | 1-x,1-y,1-z | 0.82 | 2.34 | 3.018(6) | 141.00 |
| O3W−H611···O5 | 1-x,1-y,1-z | 0.85 | 2.00 | 2.785(5) | 154.0 |
| O3W−H612···O9W | | 0.85 | 2.18 | 2.899(5) | 142.0 |
| O4W−H621···O6 | 1-x,1-y,1-z | 0.85 | 1.91 | 2.679(5) | 150.0 |
| O4W−H622···O2 | 1-x,-y,1-z | 0.85 | 2.08 | 2.907(5) | 165.00 |
| O5W−H631···O3 | 1-x,1-y,1-z | 0.86 | 2.04 | 2.803(6) | 148.0 |
| O5W−H632···O9W | 1+x,y,z | 0.86 | 1.92 | 2.773(5) | 171.0 |
| O6W−H731···O1 | -x,1-y,-z | 0.84 | 1.98 | 2.801(5) | 163.0 |
| O6W−H732···O12W | 1-x,1-y,-z | 0.86 | 2.07 | 2.791(6) | 141.0 |
| O7W−H741···O11W | 1-x,2-y,-z | 0.82 | 2.11 | 2.776(7) | 139.0 |
| O7W−H742···O6W | -x,2-y,-z | 0.82 | 2.53 | 2.856(6) | 105.0 |
| O8W−H751···O7 | -x,1-y,-z | 0.86 | 1.98 | 2.741(6) | 147.0 |
| O8W−H752···O2 | x,1+y,z | 0.85 | 1.97 | 2.817(5) | 172.0 |
| C6−H06···O3 | | 0.93 | 2.46 | 2.773(6) | 100.0 |
| C13−H014···O7 | | 0.93 | 2.48 | 2.790(6) | 100.00 |

**Table S6:** The number and nature of red spots (N) near different oxygen atoms for the anionic coordination unit along with the neighboring interacting components of the complex.

| Fragment | Atom | N | Nature | Interactions | Interacting neighbors |
|---|---|---|---|---|---|
| Coordinated carboxylate group | O1 | 1 | Deep | O1···H731–O6W | $[Mg(OH)_6]^{2+}$ (B) |
| | O2 | 3 | Deep<br>Deep<br>Deep | O2···H622–O4W,<br>O2···H752–O8W,<br>O2···H542–O10W | $[Mg(OH)_6]^{2+}$ (A)<br>$[Mg(OH)_6]^{2+}$ (B)<br>Water (C) |
| Free carboxylate group | O3 | 2 | Deep<br>Deep | O3···H541–O10W,<br>O3···H631–O5W | Water (C)<br>$[Mg(OH)_6]^{2+}$ (A) |
| | O4 | 3 | Deep<br>Light<br>Light | O4···H381–O2W,<br>O4···H562–O12W,<br>O4···H371/H372–O1W | $[Co^{II}(pdc)_2(H_2O)_2]^{2-}$<br>Water (D)<br>$[Co^{II}(pdc)_2(H_2O)_2]^{2-}$ |
| Coordinated carboxylate group | O5 | 1 | Deep | O5···H611–O3W | $[Mg(OH)_6]^{2+}$ (A) |
| | O6 | 2 | Deep<br>Deep | O6···H621–O4W,<br>O6···H552–O11W | $[Mg(OH)_6]^{2+}$ (A)<br>Water (A) |
| Free carboxylate group | O7 | 2 | Light<br>Deep | O7···H551–O11W,<br>O7···H751–O8W | Water (A)<br>$[Mg(OH)_6]^{2+}$ (B) |
| | O8 | 3 | Deep<br>Deep<br>Light | O8···H372–O1W,<br>O8···H382–O2W,<br>O8···H351–O9W | $[Co^{II}(pdc)_2(H_2O)_2]^{2-}$<br>$[Co^{II}(pdc)_2(H_2O)_2]^{2-}$<br>Water (B) |
| Coordinated water molecule | O1W | 2 | Deep<br>Light | O1W–H372···O8,<br>O1W–H371···O4 | $[Co^{II}(pdc)_2(H_2O)_2]^{2-}$<br>$[Co^{II}(pdc)_2(H_2O)_2]^{2-}$ |
| | O2W | 2 | Deep<br>Deep | O2W–H382···O8,<br>O2W–H381···O4 | $[Co^{II}(pdc)_2(H_2O)_2]^{2-}$<br>$[Co^{II}(pdc)_2(H_2O)_2]^{2-}$ |

**Table S7:** Coordination number and the neighboring moieties around different components of the complex from the fragment patch diagrams.

| Molecular/ionic units | Neighboring moieties | Primary interaction: C.N. | Total coordination number |
|---|---|---|---|
| $[Co^{II}(pdc)_2(H_2O)_2]^{2-}$ | $[Co^{II}(pdc)_2(H_2O)_2]^{2-}$ | π··· : 4 | 26 |
| | | O···H–O : 2 | |
| | $[Mg(OH)_6]^{2+}$ | O···H–O : 6 | |
| | $H_2O$ | O···H–O : 14 | |
| $[Mg(OH)_6]^{2+}$ (A) | $[Co^{II}(pdc)_2(H_2O)_2]^{2-}$ | O···H–O : 6 | 20 |
| | $[Mg(OH)_6]^{2+}$ | O···H–O : 4 | |
| | $H_2O$ | O···H–O : 10 | |
| $[Mg(OH)_6]^{2+}$ (B) | $[Co^{II}(pdc)_2(H_2O)_2]^{2-}$ | O···H–O : 6 | 20 |
| | $[Mg(OH)_6]^{2+}$ | O···H–O : 4 | |
| | $H_2O$ | O···H–O : 10 | |
| $H_2O$ (A) | $[Co^{II}(pdc)_2(H_2O)_2]^{2-}$ | O···H–O : 3 | 9 |
| | $[Mg(OH)_6]^{2+}$ | O···H–O : 3 | |
| | $H_2O$ | O···H–O : 3 | |
| $H_2O$ (B) | $[Co^{II}(pdc)_2(H_2O)_2]^{2-}$ | O···H–O : 4 | 9 |
| | $[Mg(OH)_6]^{2+}$ | O···H–O : 2 | |
| | $H_2O$ | O···H–O : 3 | |
| $H_2O$ (C) | $[Co^{II}(pdc)_2(H_2O)_2]^{2-}$ | O···H–O : 3 | 9 |
| | $[Mg(OH)_6]^{2+}$ | O···H–O : 3 | |
| | $H_2O$ | O···H–O : 3 | |
| $H_2O$ (D) | $[Co^{II}(pdc)_2(H_2O)_2]^{2-}$ | O···H–O : 4 | 8 |

| | | | |
|---|---|---|---|
| | $[Mg(OH)_6]^{2+}$ | O···H–O : 2 | |
| | $H_2O$ | O···H–O : 2 | |

**Table S8.**The effective mass of the charge carriers (EM) calculated at different high-symmetry points in the Brillouin zone (Bold letters) and the direction of carrier movement as shown in the parenthesis for the supramolecular complexes.

| **Carrier** | EM **k-point** (Direction) |
|---|---|
| $m_e^* / m_0^*$ | 11.399 **Γ**(Z → Γ)<br>51.602 **Γ** (Γ → F) |
| $m_h^* / m_0^*$ | 155.416 **F** (Γ → F)<br>14.382 **F** (F → Q) |

**IR spectroscopic characterization of the complex:**At the range of highest frequencies, the stretching vibration of non-coordinated/free –OH group ($\upsilon^{water}_{OH}$) appears in 3550 $cm^{-1}$ region. A shift of this band to lower frequency region is accepted as a criterion for the presence of hydrogen bonding interactions present in the system. In the complex under investigation the presence of coordinated water molecules is ascertained by the observation of broad double hump of stretching $\nu_{OH}$ group from water molecules, one centered around 3380 $cm^{-1}$ and another around 3178 $cm^{-1}$ which is further confirm by an additional peak at 827 $cm^{-1}$ (Figure S1).

Here the IR spectrum of the complex (Figure S1) depicts two sets of the asymmetric and symmetric mode of vibrational frequencies characteristics of C=O bond of carboxylate group in the frequency range 1607-1361 $cm^{-1}$.[19-21]The stretching frequencies observed around

1607 and 1391 $cm^{-1}$, correspond to the asymmetric and symmetric vibrational frequencies of C=O bonds of coordinated carboxylate groups present in the system, whereas the bands occurring at 1592 and 1361$cm^{-1}$ may be attributed to $\upsilon_{COO^-}^{asym}$ and $\upsilon_{COO^-}^{sym}$ vibrations of the non-coordinated carboxylate group of isocinchomeronic acid ligand present in the system. Further, the differences between bands for the asymmetric and symmetric modes of stretching vibrations of coordinated and non-coordinated $COO^-$ are 246 and 201 $cm^{-1}$, respectively. The differences $\Delta\bar{\upsilon}_{COO^-}^{chelate} > \Delta\bar{\upsilon}_{COO^-}^{ionic}$ suggest the presence of monodentate mode of coordination[19-21]for carboxylate group with $Co^{2+}$ ion in the anionic unit of the complexwhich coroborates the presence of the monodented mode of coordination/chelation of the 2,5-pdc ligands as observed in ORTEP diagram of the complex (Figure 1).

**Absorption spectroscopy in the light of crystal field theory:**

The supramolecular complexcontains octahedral $[Co(PDC)_2(2H_2O)]^{2-}$ anion in addition to charge balancing $[Mg(H_2O)_6]^{2+}$ cation, whose optical transition occur in the ultraviolet region of the electromagnetic spectrum (near 250 nm). The remaining transitions of the sample lie in the visible region of the electromagnetic spectrum and belong to the absorptions within the 3d-orbital manifold. When the electronic spectra (Figure 4) is interpreted in terms of crystal field theory coupled with the invocation of ligand based as well as metal-ligand charge transfer transitions, three ligand field bands are expected for high spin octahedral geometry of the $Co^{2+}$ ion and these bands are for the transition from the electronic ground state $^4T_{1g}(F)$ to $^4T_{2g}(F)$, $^4A_{2g}(F)$ and $^4T_{1g}(P)$ states, in order of their increasing energy. However, only two characteristic bandscorresponding to d-dtransition can be observed in the visible-NIR optical range. The first band (lowest energy) with the very low intensity in NIR region (Band maxima:$\bar{\upsilon}_1$= 8296 $cm^{-1}$) can be assigned to $^4T_{1g}(F) \rightarrow {}^4T_{2g}(F)$ transition, whereas the second

band ($\bar{\upsilon}_2$, For $^4T_{1g}(F) \rightarrow {}^4A_{2g}(F)$ transition) is absent as itis due to a two electron transition, and the third band appears in visible region (Band maxima: $\bar{\upsilon}_3$= 19381 $cm^{-1}$) due to $^4T_{1g}(F) \rightarrow {}^4T_{1g}(P)$. Another band(Band maxima: 22424 $cm^{-1}$) appears due to transition to one of the spin doublet levels, which gains intensity *via* spin orbit coupling because of its proximity to the $^4T_{1g}(P)$ state. These electronic spectral bands clearly indicate that the $[Co(PDC)_2(H_2O)_2]^{2-}$ moiety have distorted octahedral geometry and might possess $D_{4h}$ symmetry.[22,23]

Due to metal to ligand charge transfer transition (MLCT), another band appears in the UV region from low energy side (Band maxima: 28537$cm^{-1}$). At higher energy regionof the spectrum, broad absorption band with no distinct peak appears. This broad absorption band (Figure 4) can be attributed to the solid-state aggregation effect, this spectrum in UV region corresponds to the $\pi_{ring} \rightarrow \pi_{CO}$ transition[24] and the vibrational fine structures of the charge transfer ($\pi \rightarrow \pi^*$) band within the pyridine based $pdc^{2-}$ ligands of the metal organic moiety. The $\pi \rightarrow \pi^*$ band corresponds to pyridine generally appears at 38910 $cm^{-1}$ (257 nm) and in systems containing more than one pyridine/pyridine based ligands (like $pdc^{2-}$) the vibrational fine structures of the $\pi \rightarrow \pi^*$ band is a common feature of the diffuse reflectance UV spectrum.[25] The weak absorption of $[Mg(H_2O)_6]^{2+}$ moiety on the other hand does not exhibit any absorption maxima due to the absence of any chromophore within it.[26] Hence, the absorption bands in UV regions mainly correspond to the ligand centered absorptions.

The crystal field parameters were estimated from the values of $\bar{\upsilon}_1$ and $\bar{\upsilon}_3$, the position maximum intensity of the bands assigned by using the following relationship of the high spin octahedral $d^7$ complexes:

$\bar{\upsilon}_1$ $[^4T_{2g}(F) \leftarrow {}^4T_{1g}(F)] = 1/2(10Dq - 15B) + 1/2[(10Dq + 15B)^2 - 12B.10Dq]^{1/2}$

$\bar{\upsilon}_3$ $[^4T_{1g}(P) \leftarrow {}^4T_{1g}(F)] = [(10Dq + 15B)^2 - 12B.10Dq]^{1/2}$

Calculated values of the crystal field parameters are listed in Table S9.

**Table S9:** Bands assigned and crystal field parameters of the complex.

| **Spectra** | $\bar{\upsilon}_1$ **(cm$^{-1}$)** | $\bar{\upsilon}_3$ **(cm$^{-1}$)** | **Dq (cm$^{-1}$)** | **B (cm$^{-1}$)** | **Dq/B** | **β** | **β$_0$ (%)** | **C** | **A** | **LFSE (cm$^{-1}$)** |
|---|---|---|---|---|---|---|---|---|---|---|
| Solid State | 8296 | 19381 | 942 | 814 | 1.16 | 0.73 | 27 | 0.098 | 1.356 | 7536 |

Where, the relationship between the crystal field parameters are as follows:

Nephelauxetic Ratio: $\beta = B/B_0$, where, B = Racah Parameter for the $Co^{2+}$ ion in the complex, $B_0$ = Racah Parameter for the free $Co^{2+}$ metal ion in gaseous state = $B_0$ = 1117 cm$^{-1}$. Percentage covalency: $\beta_0 = (1 - \beta) \times 100$.

Ligand Field Stabilization energy (LFSE) = 8 ×Dq. And the value of the parameters c and A are given as:

$$c = 0.75 + 1.875\frac{B}{Dq} - 1.25\left[1 + 1.8\frac{B}{Dq} + \left(\frac{B}{Dq}\right)^2\right]^{1/2}$$

and $A = \dfrac{3/2 - c^2}{1 + c}$.

**Density of states from band structure analysis:**

The bands have been assigned according to density of states (DOS) (Figure S14), where the partial density of states (PDOS) coming from different type of atomic orbitals to form the total density of states (TDOS) have been shown in Figure S15. The contribution of PDOS

coming from the component units i.e., $[Mg(H_2O)_6]^{2+}$, $H_2O$ and $[Co(2,5\text{-}pdc)_2(H_2O)_2]^{2-}$ forming the total density of states of the supramolecular complex is depictedin Figure S16.

It can be observed that the inner shell VBs near -40.2 eV is formed mainly due to Mg-2p and have a large gap with the next upper bands located near -22.4 eV(Figures S14 and S15). The VBs ranging from -22 to -12.6 eV are formed due to the superposition of C-2s, C-2p, H-1s, N-2s and O-2s states. The VBs localized at -10 to -6.38 eV are mainly composed of O-2p, H-1s, C-2p states mixing with small amount of N-2p states. The VBs just below the Fermi level ranging from -6 eV to Fermi level (0 eV) are formed mostly due to contribution of C-2p, O-2p, Co-3d states mixing with a partial amount of H-1s and N-2p states, in which the top of the VBs (-1.11 eV~ 0 eV) are mainly dominated by Co-3d (8.23 electrons/eV) and O-2p orbitals (7.18 electrons/eV). The conduction bands (CBs) just above Fermi level ranging from 1.66 to 4.74 eVare formed predominantly due to the hybridization of C-2p and Co-3d orbitals mixing with slight amount of contribution coming from O-2p and N-2p states.

The contribution of PDOS from the component units i.e., $[Mg(H_2O)_6]^{2+}$, $H_2O$ and $[Co(2,5\text{-}pdc)_2(H_2O)_2]^{2-}$forming the total density of states of the supramolecular complex is depictedin Figure S16. In the PDOS diagram, some peaks are obtained at the same energy level due to hybridization between different atomic orbitals of the different moieties of the complex. This result implies that a large number of intermolecular interactions exist between different moieties within the complex. The hybridization between C-2s and O-2s is observed from -22.16 to -20.87 eV and C-2s, C-2p, N-2s, O-2s hybridize with H-1s from -20.12 to -18.60 eV (Figure S15) inferring strong intra- and inter-molecular interaction among the atoms forming the molecular/ionic units of the complex.

**Charge density and electron localization function (ELF):**

Charge-density analysis and ELF can be used to analyze the nature of chemical bonding in complex structures such as hydrogen bonded supramolecular complex (HSF). The charge density and ELF projected as iso- surface (with iso value = 0.5) on the component geometries of the complex represent the density distribution of electronic charges and the atomic bonding nature of the components respectively (Figure S18 (a) and Figure S19 (a)). To clearly visualize the charge density and ELF of the component fragments charge density and ELF are projected on different lattice planes as shown in Figure S18 and Figure S19. Charge densities in Figure S18 are plotted to show the best fit view and on lattice plane with Miller indices (0, 0, 1), (0, 1, 0) and (1, 0, 0) respectively.

The charge-density plots clearly show that each component of the complex display their usual molecule-like subunit structure individually (Figure S18(b)). Both of the ionic coordinated moieties display nearly spherical charge distributions around the metal centre along with the coordinated oxygen atoms for cationic $Mg(H_2O)_6$ and the coordinated oxygen and nitrogen atoms for anionic $Co(pdc)_2(H_2O)_2$ geometry. Moreover, for the anionic geometry the uncoordinated carboxylate oxygens show nearly spherical charge distribution. Again the absence of charge density distribution between metal and coordinated atoms sites makes ridge like regions between the metal and coordinated atoms which confirms the ionic bonding characteristics in both of the coordinated subunits of complex (Figures S18 (c), (d), (f)). The organic ligand unit of the anionic moiety shows the characteristics of normal C-C, C-O, and C-H covalent bonds (Figures S18 (b), (e)).

ELF represents the probability of finding an electron pair in the region of molecular space with $0 \leq ELF \leq 1$, can be used to elucidate the chemical bonding environment in the coordination complex. The perfect localization of an electron pair with opposite spins in a region corresponds to the value of ELF = 1 and it may form a covalent bond, lone pairs (filled core levels), or an unpaired lone electron of a dangling bond. In the region, where the value

of ELF is close to 0.5, presence of homogeneous electron gas can be evidenced and the bonding is found to have a metallic character. Again, where electrons are highly delocalized or no electron density exists (vacuum), ELF is found close to 0 in that region. It can be argued that ELF considers the concept of an electron pair as the fundamental theme of the chemical bonding theory and is mainly related to Pauli exclusion principle not the electron density.

The ELFs, plotted on different lattice planes with different Miller indices as indicated in the figure caption, are presented in Figure S19. Since for the ionic sub-units all the metal oxide bonds (Co–O/N or Mg–O) do not lie on the same plane of organic molecule the ELFs are presented on three lattice planes and also a best fit view has included to show the electron localization. The regions with color red correspond to the high localization and the blue regions indicate low localization. All ELF plots showing the large value of ELF ($\geq 0.5$) with small spherical charge localization between neighbouring C atoms indicate the strong covalent character of the C-C bond (Figures S19 (a) and (b)). Similarly, the relatively high value ($\geq 0.5$) of ELF with nearly spherical charge localization on the H atom sites shows the covalent bonding nature of C-H and O-H bonds (Figures S19 (b) and (c)). The ELF value between central metal atoms and the coordinated sites is negligible (Figures S19 (d), (e)and (f)). The moderate ELF value ($\approx 0.5$) on the O and/or N atom sites concludes the predominant bonding between Co and O/N atoms in the anionic moiety and Mg and O atoms in cationic moiety are ionic in nature (Figures S19 (a), (d) and (f)). The non-spherical charge localization around O and N atoms and between C-O/C-N bonds with ELF $\geq 0.5$ indicates local polarizability confirming the polar covalent bonding character of the C-N and carboxylate C-O bonds (Figures S19 (b) and (e)).

**Charge analysis:** The quantum chemical calculations of the atomic charges in molecular crystalline solids cannot be uniquely defined as there are various ways of partitioning the continuous electronic charge density to identify how many electrons are associated with fragments of the system such as atoms or molecules or a group of atoms in a solid.

Mulliken charge analysis is the most commonly used partitioning scheme due to its simplicity but it is considered more of a qualitative than a quantitative approach as it is highly sensitive to the choice of basis set. The result of the population analysis of the complex applying the Mulliken and Hirshfeld scheme shows that the calculated values of the Mulliken effective charges (MEC) and the Hirshfeld charges (HC) here also follow the common trend among these schemes observed in previous studies, i.e., MEC>HC.

The calculated Mulliken effective charges (MEC) of Co atoms, N atoms and O atoms in the basal plane of anionic coordination unit are close to +1.410, −0.410 and −0.640/-0.650 |e|, respectively. The charges on the O atom of the coordinated water molecules are −1.030/−1.040 |e|. Similarly for the cationic coordination unit the calculated MEC for Mg atoms are close to +2.000/2.020 |e| and for and O atoms the charges are fairly consistent and vary slightly between −1.090 to −1.150 |e|. Such a population distribution indicates the partial electron transfer from Co atom to O and N atoms and Mg atom to O atom, establishing the ionic character of the coordination environments. The carboxylate C atoms that connect to the O atoms bear positive charges and all other C atoms have negative charges. The positive charges of marginal C atoms are fairly consistent and vary slightly between +0.53 to +0.61. All O atoms of the anionic unit carry negative charges and vary in the range of -0.52 to -0.81 |e|. The resulting charges are +1.64 |e| on the cationic unit and −1.64 |e| on the anionic unit.

The population analyses with Hirshfeld scheme show similar characteristics to Mulliken analysis. The Bader atomic charges of Co, N and O in the basal plane of anionic coordination unit are about +0.280 |e|, −0.070/-0.060 |e| and -0.210/-0.200 |e|, respectively.

These results indicate that the interaction between Co and N/O is ionic. The resulting charges are +0.81 |e| on the cationic unit and −0.79 |e| on the anionic unit. The population analysis result tallies well with the charge density and ELF analyses.

**Anomalous Dielectric response (323 K-353 K):** While recording the frequency dependent dielectric data above 313 K (40 °C) it has been observed that the impedance spectra (Nyquist plot) show similar plot as measured in the temperature range of 278 K to 313 K, but now the radius of the semi-circular plots are abruptly increasing with the rise of temperature (Figure S20 (a)). In case of conductivity spectra (σ') there observed abrupt decrease with rise of temperature. The hopping frequency (transition frequency from dc to ac region) seems to be shifted to lower frequency with the increase of temperature (Figure S20 (b)).

Upto 313 K the material exhibit semiconducting nature whose impedance decreases and conductivity rises with increase of temperature and the material follows Arrhenius type thermal dependency. The impedance and dielectric data can be analyzed according to cole-cole model. But after reaching 313 K material started to behave completely opposite. It can be assumed that the number of carries start to decrease gradually with increase of temperature above 313 K resulting the above observations. Again from the thermal plot it can be observed that with gradual increase of temperature the lattice water molecules first started to deplete from the framework after 315K. These observations point to the fact that the protons supplied by the coordinated water molecules serve as the charge carriers for dielectric measurements and they are transferred through the material by guest water mediated hydrogen bonding interactions such that as the water molecules start to flee from the framework, the numbers of carries decreases also the hydrogen bonded pathway get ruptured.

**Electrical characterization:**

**Four probe technique:**

The values dc-resistivity of the complex (in pellet form) at some selected temperatures was recorded using the four probe technique in the temperature range of 5-40 °C, which showed Arrhenius type temperature dependence (Figure S23).

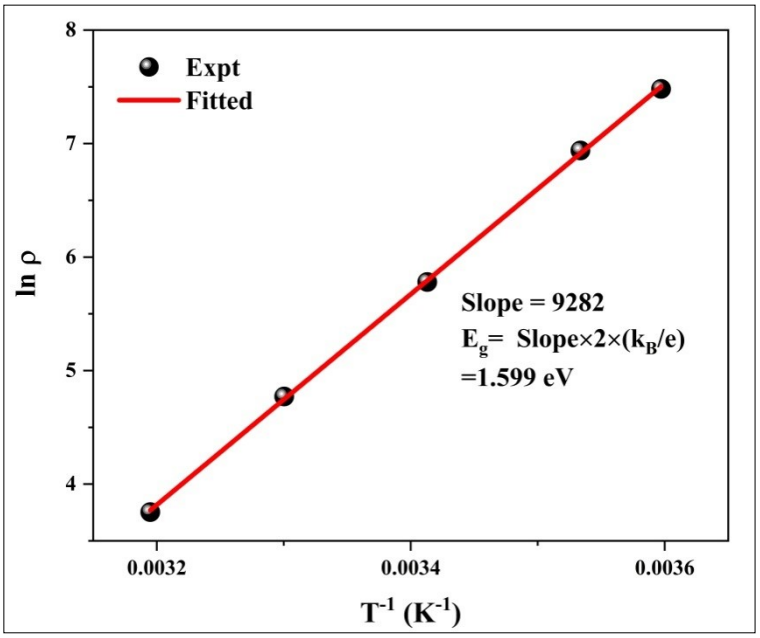


**Figure S23:** Arrhenius-type behavior of the dc-resistivity measured by four probe method.

**IV measurement on ITO/complex/Al device:**

Again the I-V curves of the ITO/complex/Al device under dark condition and visible light irradiation obey the equation $I = C_1\, exp\,(-C_2)\left[exp(C_3V) - 1\right]$, where $C_1$, $C_2$ and $C_3$ are constants that depend on different parameters of the device,portraying the thermionic emission behaviour of Schottky barrier diode(Figure S24).

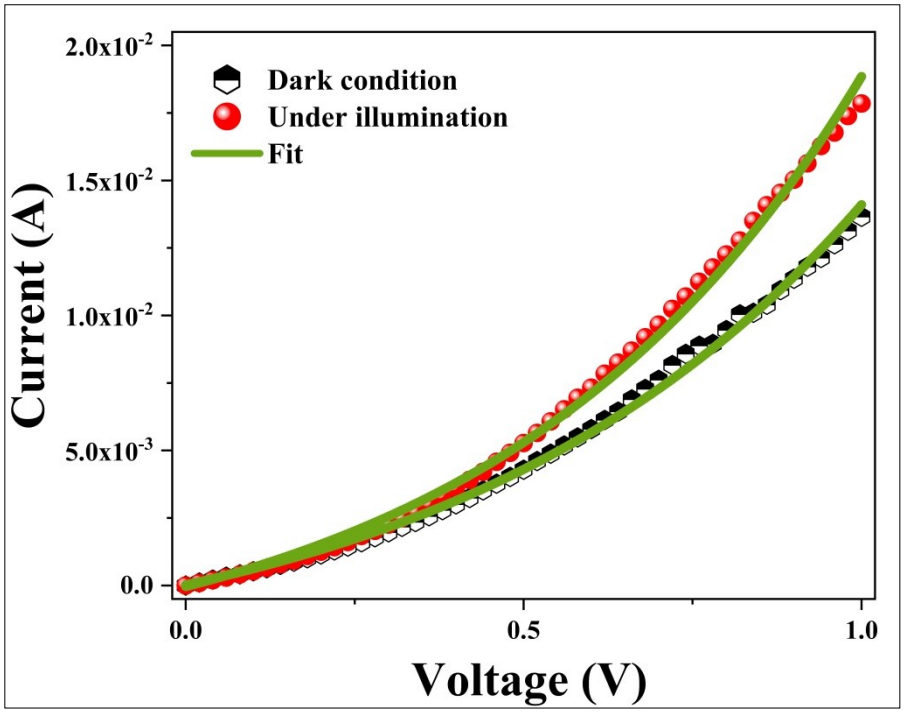


**Figure S24:** The I-V characteristics of the ITO/complex/Al device under the application of forward bias fitted under thermionic emission theory.

**Photoresponsive behavior of the complex under thermionic emission theory:**

The *I–V* characteristic of the complex based SBD has been analyzed by thermionic emission theory and Cheung's method was employed to extract important diode parameters.[27]In this regard, we have analysed *I–V* curves quantitatively by considering the following standard equations:[27,28]

$$I = I_0\, exp\left(\frac{qV}{\eta kT}\right)\left[1 - exp\left(\frac{-qV}{\eta kT}\right)\right] \quad (1)$$

$$I_0 = AA^{*}T^2 exp\left(\frac{-q\emptyset_B}{kT}\right) \quad (2)$$

where $I_0$, $k$, $T$, $V$, $A$, $\eta$ and $A^*$ stands for saturation current, electronic charge, Boltzmann constant, temperature in Kelvin, forward bias voltage, effective diode area, ideality factor and effective Richardson constant, respectively. The effective diode area has been estimated as $7.065 \times 10^{-2}$ $cm^2$ and the effective Richardson constant has been considered as 32 $AK^{-2}\,cm^{-2}$ for all the devices.

We have also determined the series resistance, ideality factor and barrier potential height by using equations (3)−(5), which has been extracted from Cheung's model,[29,30]

$$\frac{dV}{dln(I)} = \left(\frac{\eta kT}{q}\right) + IR_S \tag{3}$$

$$H(I) = V - \left(\frac{\eta kT}{q}\right)\ln\left(\frac{I_S}{AA^*T^2}\right) \tag{4}$$

$$H(I) = IR_S + \eta\emptyset_B \tag{5}$$

From the intercept of dV/dlnI versus I plot (Figure S25) the ideality factor (η) for all devices under both conditions has been determined whereas the slope of this plot represents the series resistance ($R_S$) of the devices. The obtained value of ideality factor for the device both under dark and irradiation conditions are listed below in Table S10. The values of ideality factor ($\eta$) have been estimated as 1.81 under dark condition for compoundbased SBD. Under photo illumination condition the same has been estimated as 1.50. The obtained values of ideality factors of the device under both the conditions represent a deviation from its ideal value (~1). This may be due to the presence of inhomogeneities of Schottky barrier height and existence of interface states and series resistance at the junction.[31,32] However, under irradiation condition the value of ideality factor approaches more ideal (closer to 1), which is a significant observation. In general, it depicts the fewer number of recombination of interfacial charge carriers and generation of better homogeneity at the barrier of Schottky junctions.[27] From this, it may be concluded that our complex based device possesses less

carrier recombination at the junction i.e. better barrier homogeneity under photo irradiation condition than.

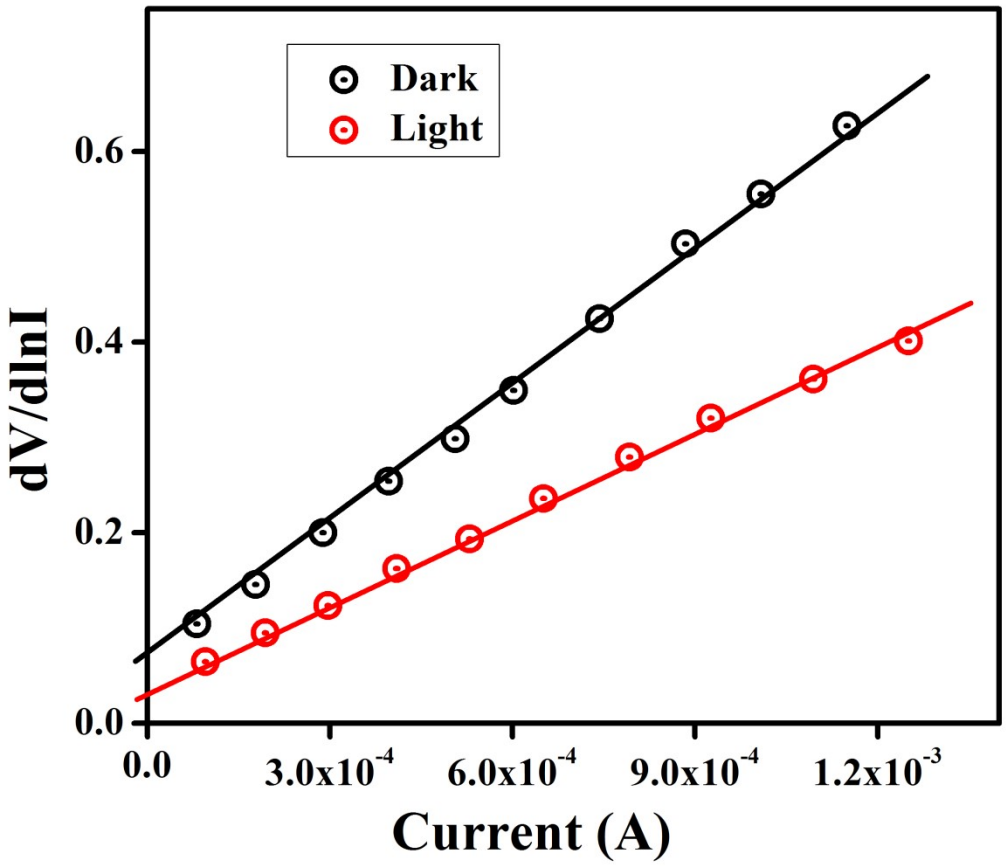


**Figure S25:** dV/dlnI vs. I curve for the compound based thin film device under dark, and photoillumination condition.

From the intercept of H(I) vs. I plot (Figure S26) and using the calculated ideality factor ($\eta$) values, the value of barrier height ($^{\emptyset}{}_{B}$) has been determined [equation (5)].

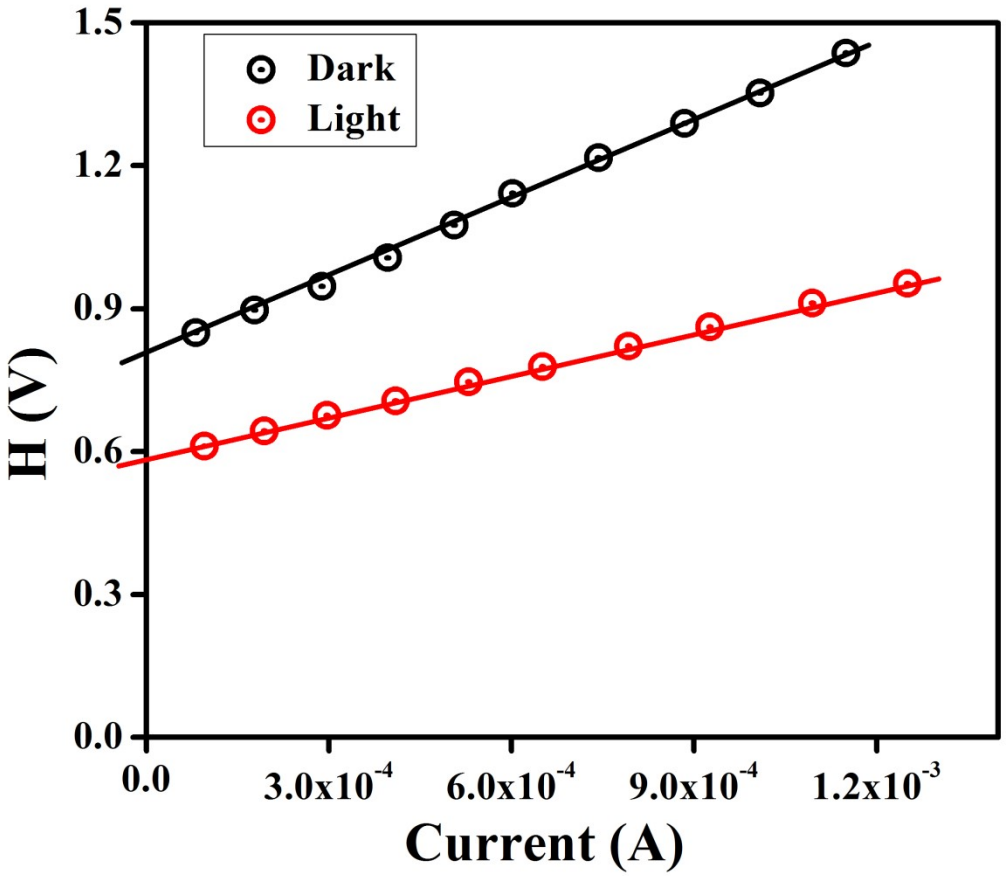


**Figure S26:** *H vs. I* curves for the compound based thin film devices under dark, and photo illumination condition.

The significant observation is that the barrier potential height of the device is reduced under irradiation condition. The generation of photo induced charge carriers and their accumulation near the conduction band may be the main reason for this diminution. The series resistance ($R_S$) of the device can also be determined from the slope of this plot. The measured potential height ($\phi_B$), ideality factor ($\eta$) and series resistance ($R_S$) under dark and illumination condition for the metal (Al)–semiconductor (synthesized compound) (MS) junction are listed in Table S10. The series resistance obtained from both processes show good consistency. The obtained series resistance is found to decrease upon light illumination (Table S10), which signifies its applicability in the field of optoelectronics devices.

**Table S10: Schottky device parameters of compound based SBD**

| Condition | On/Off | Conductivity ($S.m^{-1}$) | Photo sensitivity | Ideality factor | Barrier height (eV) | $R_S$ From dV/dln I (Ω) | $R_S$ from $H$ (Ω) |
|---|---|---|---|---|---|---|---|
| Dark | 13.05 | $2.43 \times 10^{-3}$ | 1.34 | 1.81 | 0.43 | 524.83 | 556.42 |
| Light | 34.27 | $3.29 \times 10^{-3}$ | | 1.50 | 0.39 | 296.13 | 295.96 |

**References:**


1. *SHELXS 97, Program for Structure Solution*, Sheldrick, G. M. University of Göttingen, Germany, **1997**.
2. *SHELXL 97, Program for Crystal Structure Refinement*, Sheldrick, G. M. University of Göttingen, Germany, **1997**.
3. Spek, A. L. Single-crystal structure validation with the program PLATON. *J. Appl.Crystallogr.,***2003**, *36*, 7–13.
4. Farrugia, L. J. ORTEP-3 for Windows - a version of ORTEP-III with a Graphical User Interface (GUI). *J. Appl. Crystallogr.,* **1997**, *30*, 565.
5. Farrugia, L. J. WinGX suite for small-molecule single-crystal crystallography. *J. Appl. Crystallogr*.,**1999**, *32*, 837–838.
6. Turner, M. J.; Mckinnon, J. J.; Wolff, S. K.;Grimwood, D. J.; Spackman, P. R.;Jayatilaka, D. and Spackman, M. A. **2017**, Crystal Explorer 17, The University of Western Australia.
7. Tan, S. L.;Jotani, M. M. and Tieknik, E. R. T. Utilizing Hirshfeld surface calculations, non-covalent interaction (NCI) plots and the calculation of interaction energies in the analysis of molecular packing, *ActaCryst.*, **2019**, *E75*, 308–318.
8. Turner, M. J.; Grabowsky, S.;Jayatilaka, D. and Spackman, M. A. Accurate and Efficient Model Energies for Exploring Intermolecular Interactions in Molecular Crystals, *J Phys Chem Lett.*, **2014**, *5*, 4249-4255.
9. Mackenzie, C. F.; Spackman, P. R.; Jayatilaka, D.; and Spackman, M. A. Crystal Explorer model energies and energy frameworks: extension to metal coordination compounds, organic salts, solvates and open-shell systems, *IUCrJ*, **2017**, *4*, 575–587.

10. Clark, S. J.; Segall, M. D.; Pickard, C. J.; Hasnip, P. J.; Probert, M. J.; Refson, K.; Payne, M. C. First principles method using CASTEP. *Z. Kristallogr.,* **2005**, *220*, 567–570.
11. C. F. Guerra, J.-W. Handgraaf, E. J. Baerends and F. M. Bickelhaupt, J. Comput. Chem., 2004, 25, 189.
12. Perdew, J. P.; Burke, K.; Ernzerhof, M. Generalized gradient approximation made simple. *Phys. Rev. Lett.,***1996**, *77*, 3865–3868.
13. Perdew, J. P.; Ruzsinszky, A.; Csonka, G. I.; Vydrov, O. A.; Scuseria, G. E.; Constantin, L. A.; Zhou, X. and Burke, K. Restoring the Density-Gradient Expansion for Exchange in Solids and Surfaces, Phys. Rev. Lett., **2008**, *100*, 136406.
14. Vanderbilt, D. Soft self-consistent pseudopotentials in a generalized eigenvalue formalism. *Phys. Rev. B.*,**1990**, 41, 7892–7895.
15. Monkhorst, H. J.; Pack, J. D. Special points for Brillouin-zone integrations. Phys. Rev. B.,**1976**, 13, 5188-5192.
16. Grimme, S. Semiempirical GGA-type density functional constructed with a long-range dispersion correction. *J. Comput. Chem.*, **2006**, 27, 1787-1799.
17. Ephraim Babu, K.; Veeraiah, A.; Tirupati Swamy, D. and Veeraiah, V. First-Principles Study of Electronic Structure and Optical Properties of Cubic Perovskite $CsCaF_3$. *CHIN. PHYS. LETT.*, **2012**, 29, 117102.
18. Yang, L. -M.; Ganz, E.; Svellec S. and Tilset, M. Computational exploration of newly synthesized zirconium metal–organic frameworks UiO-66, -67, -68 and analogues. *J. Mater. Chem. C*, **2014**, 2, 7111–7125.
19. Lewandowski, W.; Kalinowska, M. and Lewandowska, H.The influence of metals on the electronic system of biologically important ligands. Spectroscopic study of benzoates, salicylates, nicotinates and isoorotates. Review,*J. Inorg. Biochem.*, **2005**, *99*, 1407-142.
20. Nara, M.; Torii, H. and Tasumi, M. Correlation between the Vibrational Frequencies of the Carboxylate Group and the Types of Its Coordination to a Metal Ion: An ab Initio Molecular Orbital Study, *J. Phys. Chem.*, **1996**, *100*, 19812-19817.
21. Deacon, G. B. and Phillips, R. RELATIONSHIPS BETWEEN THE CARBON-OXYGEN STRETCHING FREQUENCIES OF CARBOXYLATO COMPLEXES AND THE TYPE OF CARBOXYLATE COORDINATION, *J. Coord. Chem. ReV.*, **1980**, *33*, 227-250.

22. Bernalte-García, A.; García-Barros, F. J.; Higes-Rolando, F. J.; Luna-Giles, F.; Pacheco-Rodríguez, M. M. and Viñuelas-Zahínos, E. Synthesis and characterization of a new cobalt(II) complex with 2-(2-pyridyl)imino-N-(2-thiazolin-2-yl)thiazolidine (PyTT), BioinorgChem Appl., **2004**, *2*, 307–316.
23. Figgis, B. N. and Hitchman, M. A. *Ligand Field Theory and Its Applications*, New York: Wiley-VCH, 2000.
24. Wasylina, L.; Kucharska, E.; Weglinski, Z. and Puszko, A. THE $^{13}C$ NMR, UV AND IR ABSORPTION SPECTRA OF PYRIDINEDICARBOXYLIC ACIDS, *ChemHeterocyclCompd*, **1999**, *35*, 186–194.
25. Das, B. K.; Bora, S. J.; Chakrabortty, M.; Kalita, L.; Chakraborty, R. and Barman,R. Structural, thermal and spectroscopic properties of supramolecular coordination solids, *J. Chem. Sci.*, **2006**, *118*, 487–494.
26. Sieranski, T. and Kruszynski, R.Magnesium sulphate complexes with hexamethylenetetramine and 1,10-phenanthroline Thermal, structural and spectroscopic properties, *J Therm Anal Calorim*, **2012**, *109*, 141–152.
27. Dey, A.; Middya, S.; Jana, R.; Das, M.; Datta, J.; Layek, A. and Ray, P. P. Light induced charge transport property analysis of nanostructured ZnS based Schottky diode, *J. Mater. Sci. Mater. Electron.*, **2016**, *27*, 6325–6335.
28. Rhoderick, E. H. *Metal–Semiconductor Contacts*, Oxford University, Press, London, 1978.
29. Cheung, S. K. and Cheung N. W. Extraction of Schottky diode parameters from forward current-voltage characteristics. *Appl. Phys. Lett*., **1986**, *49*, 85-87.
30. Dey, A.; Layek, A.; Roychowdhury, A.; Das, M.; Datta, J.; Middya, S.; Das, D. and Ray, P. P. Investigation of charge transport properties in less defective nanostructured ZnO based Schottky diode. *RSC Adv.,* **2015**, *5*, 36560–36567.
31. Gupta, R. K. and Yakuphanoglu, F. Photoconductive Schottky diode based on Al/p-Si/$SnS_2$/Ag for optical sensor applications. *Sol. Energy,* **2012**, *86*, 1539–1545.
32. Jana, R.; Dey, A.; Das, M.; Datta, J.; Das, P. and Ray, P. P. Improving performance of device made up of CuO nanoparticles synthesized by hydrothermal over the reflux method, *Appl.Surf.Sci*,.**2018**, *452*,155-164.